Structural and Functional Characterization of the Bestrophin-2 Anion Channel

Aaron P. Owji[1,#], **Qingqing Zhao**[2,3,#], **Changyi Ji**[2], **Alec Kittredge**[2], **Austin Hopiavuori**[2], **Ziao Fu**[4], **Nancy Ward**[2], **Oliver B. Clarke**[5], **Yin Shen**[3,*], **Yu Zhang**[6,*], **Wayne A. Hendrickson**[4,5,7,*], **Tingting Yang**[2,6,*]

[1]Department of Pharmacology, Columbia University, New York, New York, USA

[2]Department of Pharmacology and Physiology, University of Rochester, School of Medicine and Dentistry, Rochester, New York, USA

[3]Eye Center, Renmin Hospital of Wuhan University, Wuhan, Hubei, China

[4]Department of Biochemistry and Molecular Biophysics, Columbia University, New York, New York, USA

[5]Department of Physiology and Cellular Biophysics, Columbia University, New York, New York, USA

[6]Department of Ophthalmology, Columbia University, New York, New York, USA

[7]New York Structural Biology Center, New York, New York, USA

Abstract

The bestrophin family of calcium (Ca^{2+})-activated chloride (Cl^-) channels, which mediate the influx and efflux of monovalent anions in response to the levels of intracellular Ca^{2+}, comprises four members in mammals (Best1-4). Here we report cryo-EM structures of bovine Best2 (bBest2) bound and unbound by Ca^{2+} at 2.4 Å and 2.2 Å, respectively. The bBest2 structure highlights four previously underappreciated pore-lining residues specifically conserved in Best2, but not in Best1, illustrating the differences between these paralogs. Structure-inspired electrophysiological analysis reveals that, although the channel is sensitive to Ca^{2+}, it has substantial Ca^{2+}-independent activity for Cl^-, reflecting the opening at the cytoplasmic restriction of the ion conducting pathway even when Ca^{2+} is absent. Moreover, the ion selectivity of bBest2 is controlled by multiple residues including those involved in gating.

*Correspondence: Tingting Yang, ty2190@cumc.columbia.edu, Wayne A. Hendrickson, wah2@cumc.columbia.edu, Yu Zhang, yz3802@cumc.columbia.edu, Yin Shen, yinshen@whu.edu.cn.
#These authors contributed equally to this work

Author Contributions

A.P.O. designed research, performed protein purification and cryo-EM experiments, analyzed data, made figures and helped with writing the paper; Q.Z. and C.J. performed and analyzed patch clamp recordings, A.K. made constructs and purified proteins, A.H. maintained cells, Z.F. helped with collecting and analyzing cryo-EM data, N.W. made viruses; O. B. C. helped cryo-EM data processing; Y.S. supervised Q.Z. and edited manuscript; Y.Z. screened and purified proteins, and wrote the paper; W.A.H. designed research and analyzed data; T.Y. designed research, analyzed data, made figures and wrote the paper.

Competing Interests Statement

The authors declare no conflict of interest.

Introduction

The bestrophin proteins are widely distributed, with representatives in most metazoans including four in humans (hBest1–4), and also in other eukaryotes and prokaryotes[1,2]. Although four bestrophin paralogs have been identified as members of the same family of Ca^{2+}-activated Cl^- channels[3,4], their channel properties and physiological functions differ. For instance, Ca^{2+}-independent activation has been reported for hBest2 but not hBest1[1]. Physiologically, Best1 is predominantly expressed in the retinal pigment epithelium (RPE) of mammals[5–7], and mutations in the human *BEST1* gene have been genetically linked to retinal degenerative disorders[6–14]. By contrast, Best2 is localized to the basolateral plasma membrane of nonpigmented ciliary epithelial (NPE) cells in mice and humans[15,16]. Best2^{−/−} mice exhibit changes in ocular aqueous flow and drainage, resulting in a reduction in intra-ocular pressure (IOP)[15]. As high IOP is a major risk factor of glaucoma, and lowering IOP slows progression at both the early and late stages of the disease[17–19], Best2 represents a potential pharmaceutical target for glaucoma. Moreover, Best2 has been suggested to regulate HCO_3^- transport in colonic goblet cells and sweat glands[20,21], reflecting the versatility of anion-selective channels in conducting different anions and the physiological importance of Best2. Therefore, a comprehensive characterization of Best2 holds tremendous biomedical value.

Among all bestrophins, only the structures of two Best1 homologs, one from the bacterium *Klebsiella pneumoniae* (KpBest) and the other from chicken (cBest1), have been solved in previous studies[22,23]. Both structures show that the pentameric Best1 channel has a flower vase-shaped ion conducting pathway that protrudes ~50 Å into the cytosolic domain. The ion conducting pathway has two narrow restrictions, one (the "neck") formed by three conserved hydrophobic residues at the transmembrane pore, and the other (the "aperture") formed by a single residue located at the cytoplasmic exit, approximately 50 Å below the transmembrane region. Compelling evidence suggest that the neck and aperture play critical roles in channel gating and anion selectivity[22–24]. Sequence alignment between Best1 and Best2 homologs indicates a high level of conservation in the neck, which is formed by the same set of residues (I76, F80 and F84) in cBest1, hBest1, hBest2 and bovine Best2 (bBest2). By contrast, the residue at the aperture varies among homologs: V205 in cBest1, I205 in hBest1, S205 in hBest2 and mBest2, and G205 in bBest2. Notably, the similarity between Best1 and Best2 in their primary sequences is not particularly high, as the sequence identity shared by hBest1 and hBest2 is 44% overall, and 60% in their transmembrane regions excluding the variable C-termini. Therefore, Best2 may have some unique structural features not seen in Best1.

Here, we solved the high-resolution cryo-EM structures of bBest2 in the Ca^{2+}-bound and Ca^{2+}-unbound states, at 2.4 Å and 2.2 Å, respectively, providing the first Best2 and the first mammalian bestrophin structure. Remarkably, the bBest2 structure displays two distinct features along the ion conducting pathway: firstly, despite conserved hydrophobic residues at the neck, the aperture-forming residue dramatically changes from a hydrophobic I or V in Best1 (KpBest I180 and cBest1 V205, respectively) to a positively charged K208 connecting to a negatively charged E212 through a salt bridge in bBest2; secondly, two positively

charged pore-facing residues- K265 and H91, form new structural landmarks in bBest2. Moreover, structure-inspired electrophysiological characterization of bBest2 revealed that the aperture is a size-sensitive Ca^{2+}-activated gate that contributes to Best2's unique Ca^{2+}-independent activity, while both K265 and H91, together with the neck and aperture, are involved in ion selectivity of the channel.

Results

Cryo-EM structures of bovine Best2

Previously, we purified bBest2 containing amino acids 1–406 (bBest2$_{1-406}$), which has 91% sequence identity with hBest2 (Supplementary Fig. 1), and showed that bBest2$_{1-406}$ is sufficient to conduct Cl^- current at median Ca^{2+} concentration[25]. To elucidate the architecture of Best2 channels, we solved the cryo-EM structures from bBest2$_{1-406}$ under three Ca^{2+} conditions: no (EGTA only), low (250 nM) and high (5 mM) Ca^{2+} (Figure 1a–d, Table 1, Extended Data Fig. 1–5 and Supplementary Fig. 2).

From a nominally Ca^{2+}-free condition, we solved two distinct states, one at 2.2 Å and another at 2.3 Å, both of which lacked a Ca^{2+} ion in the known Ca^{2+} binding site. The high resolution of these maps revealed carbonyl groups, allowed placement of water molecules, and facilitated unambiguous assignment of most side chains (Figure 1c). From the high Ca^{2+} condition, we solved one state at 2.4 Å, which was bound by Ca^{2+}. From the low Ca^{2+} condition, two states were identified and solved at 3.0 Å resolution, one similar to a Ca^{2+}-unbound state and the other identical to the high Ca^{2+} state (Table 1, Extended Data Fig. 1–5 and Supplementary Fig. 2).

Overall, the structures are very similar to one another (root-mean-square deviation (RMSD) = 0.3 Å for Ca^{2+}-unbound vs. -bound states from the low Ca^{2+} condition), and resemble the previously solved cBest1 and KpBest (RMSD = 0.6 Å comparing Ca^{2+}-bound bBest2 to Ca^{2+}-bound closed cBest1, Fig. 1d and Extended Data Fig. 4a), indicating a high level of conservation in the architecture of bestrophins. Residues 75–91 in the second transmembrane domain line the ion conducting pore, reaffirming previous electrophysiological results which predict a critical involvement of this helix in pore function (Supplementary Fig. 1)[26–28].

Similar to the KpBest and cBest1 structures, bBest2 showed two major permeation constrictions in the ion conducting pathway: the neck and aperture (Fig. 1d). Remarkably, although the neck is formed by the same set of hydrophobic residues (I76, F80 and F84) in bBest2 and cBest1 with similar radii, neither position nor composition of the aperture is conserved: a positively charged K208 together with a negatively charged E212 form the tightest constriction to the ion conduction pathway within the cytosolic region of bBest2, in sharp contrast to the hydrophobic aperture formed by V205 in cBest1 and I180 in KpBest (Fig. 1d–e). Moreover, the side chains of two positively charged residues, K265 and H91, point to the ion conducting pore and form additional constrains (Fig. 1d–e). Notably, these four residues are highly conserved in Best2, but not in Best1, Best3 or Best4.

The Ca²⁺-sensing apparatus

Based on the bBest2 structures, three regions undergo Ca^{2+}-dependent ordering: 1) a conserved Ca^{2+}-clasp previously identified in the cBest1 crystal structure, consisting of a cluster of acidic residues (E300, D301, D302, D303 and D304) within a tight turn between helix S4a and S4b (Supplementary Fig. 1, and Extended Data Fig. 4a, 4c and 5b); 2) residues 2–23, comprising helix S1a and S1b (the "N-terminal extension", Supplementary Fig. 1, and Extended Data Fig. 4b and 5a); 3) the C-terminal extension, which includes residues 340–368, and extends around the midsection of the cytosolic domain, past the adjacent protomer, making contact with the next protomer over (Supplementary Fig. 1, and Extended Data Fig. 4d and 5c). All three regions are well-ordered in the Ca^{2+}-bound state and partially or completely disordered in the Ca^{2+}-unbound states (Extended Data Fig. 4b–d and 5a–c). The first two regions are in direct contact with Ca^{2+}, which is coordinated by the acidic side chains from D301 and D304 of the Ca^{2+}-clasp and by the backbone carbonyl oxygen atoms from A10 and Q293.

Ca^{2+} binding also stabilizes the transmembrane region, as the local resolution (Extended Data Fig. 1–3), especially of helix S1c which is immediately adjacent to the Ca^{2+}-dependent S1a and S1b, is of higher quality in the Ca^{2+}-bound state compared to Ca^{2+}-unbound states. It is likely that Ca^{2+}-dependent stabilization of the N-terminal extension anchors S1c, ordering it and constraining the transmembrane region.

Ca²⁺-dependent and independent activities of Best2

Ca^{2+}-independent channel activity has been reported for hBest2[1], but not for any of the other bestrophin homologs, suggesting a distinctive characteristic of Best2 channels. However, the data supporting Ca^{2+}-independent activity of hBest2 were not shown, while Best2 has never been compared side by side with Best1 in both the absence and presence of Ca^{2+}. To address these deficits, WT hBest1 and hBest2 were individually introduced into HEK293 cells, which do not have any endogenous Ca^{2+}-activated Cl^- channels on the plasma membrane[29], and subjected to whole-cell patch clamp. Both hBest1 and hBest2 conducted Cl^- currents which were significantly enhanced by 1.2 μM intracellular Ca^{2+} ($[Ca^{2+}]_i$) compared to those at 0 $[Ca^{2+}]_i$, respectively (Fig. 2a–d). Importantly, hBest2 displayed robust current even at 0 $[Ca^{2+}]_i$ (54 ± 18 pA/pF, Fig. 2d and 2h), in sharp contrast to the tiny current by hBest1 which did not differ significantly from untransfected control under this condition (4 ± 1 pA/pF, Fig. 2b and 2h). Therefore, unlike hBest1 whose channel activity absolutely requires Ca^{2+}, hBest2 is partially functional even in the absence of Ca^{2+}.

To test whether bBest2 also has Ca^{2+}-independent activity, WT bBest2 and C-terminus truncated bBest2$_{1–406}$ were individually transfected into HEK293 cells for patch clamp. Consistent with results from hBest2, both bBest2 and bBest2$_{1–406}$ conducted significantly bigger currents at 0 $[Ca^{2+}]_i$ (13 ± 4 pA/pF vs. 18 ± 6 pA/pF) compared to untransfected controls (2 ± 0.5 pA/pF, Fig. 2e–h), and the currents dramatically increased in amplitude as $[Ca^{2+}]_i$ was raised to 1.2 μM (Fig. 2f–h).

The structure models suggest distinct apertures in Best1 and Best2. To functionally verify this difference, we swapped the residue 205 by generating hBest1 I205S and I205G

(mimicking hBest2 and bBest2, respectively), and hBest2 S205I and bBest2 G205I (mimicking hBest1). Mutant channels were individually expressed in HEK293 cells and tested by patch clamp. Cells overexpressing hBest1 I205S or I205G died quickly after incubating in patch external solution, suggesting that the mutant channels were constantly open. By contrast, cells expressing hBest2 S205I or bBest2 G205I conducted currents similar to their WT counterparts in the absence of Ca^{2+}, but the currents could no longer be stimulated by Ca^{2+} (Extended Data Fig. 6a–c). These results clearly indicate that Best1 and Best2 have different gating mechanisms at the aperture, in accord with the structural models (Fig. 1d).

Ca^{2+}-sensitivity and ion selectivity of bBest2

To profile the Ca^{2+}-sensitivity of bBest2, we performed patch clamp in HEK293 cells transiently transfected with bBest2 across a range of free $[Ca^{2+}]_i$. As expected, the amplitudes of recorded Cl^- currents were apparently sensitive to $[Ca^{2+}]_i$ (Fig. 3a–b). A plot of peak current (evoked with a +100 mV step pulse) as a function of $[Ca^{2+}]_i$ displayed robust Ca^{2+}-dependent activation with the Ca^{2+} half maximal effective concentration (EC_{50}) at 26 nM (Fig. 3b), which is comparable with that of cBest1, but much smaller than that of mBest2 (230 nM) or Xenopus Best2 (xBest2, 210~228 nM)[24,27,30].

To characterize the ion selectivity of bBest2 to different anions, we measured the reversal potentials (E_{rev}) with 120 mM Cl^- in the intracellular solution and 120 mM Cl^-, Br^-, I^-, or SCN^- in the extracellular solution. Notably, when Cl^- was in the extracellular solution, the measured E_{rev} (-1.2 ± 0.6 mV) was very close to the theoretical E_{rev} (0 mV) calculated by Nernst equation, validating our experimental setup. The E_{rev}s for Br^-, I^- and SCN^- indicated the same anionic permeability order of $SCN^- > I^- > Br^- > Cl^-$ as that of mBest2 and cBest1 (Fig. 3c and Extended Data Fig. 6d–h)[24,27]. The permeability of an ion reflects the ease with which the ion enters the channel[27]. The permeability ratios in relative to Cl^- (P_X/P_{Cl}), calculated by the shift in E_{rev} of the current under bi-ionic conditions, were 8.00 for SCN^-, 1.99 for I^-, and 1.23 for Br^- (Fig. 3d), very similar to these of mBest2 but noticeably lower than these of cBest1[24,27]. Moreover, bBest2 also exhibited a much higher relative permeability to cation ($P_{Na}/P_{Cl} = 0.45$, Fig 3c–d), compared to hBest1 ($P_{Na}/P_{Cl} = 0.03$) and cBest1 ($P_K/P_{Cl} = 0.05$)[23,24]. Together, these results indicate that Best2 channels are generally less ion-selective than Best1 channels.

Although the substitution of extracellular Cl^- with Br^-, I^-, or SCN^- all caused a shift of E_{rev} towards the same direction (Fig. 3c–d), the influence on the channel conductance, which reflects the interaction of the permeant ion with the channel[27], was very different. In particular, the current amplitude was enhanced by Br^-, unaltered by I^-, and reduced by SCN^- (Fig. 3c), suggesting that the relative conductivity of bBest2 for anions is $Br^- > I^- = Cl^- > SCN^-$, distinct from that of cBest1 ($SCN^- > I^- > Br^- > Cl^-$) or mBest2 ($I^- > Br^- > Cl^- > SCN^-$)[24,27]. Interestingly, the conductance of bBest2 in both inward and outward directions was dramatically increased by extracellular Br^-, but reduced by extracellular SCN^- (Fig. 3c), suggesting that Br^- and SCN^- have a positive and negative influence in bBest2 conductance, respectively.

The neck, but not the aperture, is a Ca^{2+}-dependent gate for Cl$^-$

We recently showed that both the neck and aperture in hBest1 are Ca^{2+}-dependent gates for Cl$^{-[31]}$. To investigate their roles in bBest2 channel gating, we performed alanine substitution for the residue(s) at the neck (I76A/F80A/F84A, 3A) or the aperture (K208A) (Fig. 4a–b). As alanine has a much shorter side chain compared to isoleucine, phenylalanine or lysine, the substitution is predicted to impair channel gating at the corresponding restriction by mimicking a constantly open state, allowing us to separate the function of the two restrictions. Mutant channels were individually expressed in HEK293 cells and tested by patch clamp. The mutants were comparable to the WT in both overall and membrane expression levels (Extended Data Fig. 7). Remarkably, 1.2 μM [Ca^{2+}]$_i$ significantly stimulated the current from the K208A mutant, but the current from the 3A mutant was substantial even without Ca^{2+} and irresponsive to Ca^{2+} (Fig. 4a–b), suggesting that only the neck, but not the aperture, functions as a Ca^{2+}-dependent gate for Cl$^-$. Moreover, the K208A mutant was indistinguishable from the WT in terms of current amplitude and Ca^{2+}-dependence (Fig. 4b and 4e), again suggesting that the aperture is not a gate for Cl$^-$ (Extended Data Fig. 8a). Consistent with this idea, both the Ca^{2+}-bound and Ca^{2+}-unbound bBest2 structures capture a bound ion density within the aperture at the level of K208, possibly representing the passing Cl$^-$ (Fig. 4c and Extended Data Fig. 9). To further investigate the aperture, we made an alanine substitution at E212, which forms a salt bridge with K208 and may be important for maintaining the open position of K208 (Fig. 4c). Interestingly, the E212A mutant conducted Cl$^-$ currents significantly larger than those from untransfected controls and similar to those from WT bBest2 in the absence of Ca^{2+}, but could no longer be stimulated by Ca^{2+} (Fig. 4d–e). This suggests a critical role of E212 in controlling the size of the aperture, possibly by pulling K208 away from the central axis and maintaining dilation at the cytosolic restriction in the presence of Ca^{2+}.

The aperture, but not the neck, is a Ca^{2+}-dependent gate for CH$_3$SO$_3^-$

We recently found that hBest1 conducts the big anion methanesulfonate$^-$ (CH$_3$SO$_3^-$)$^{[31]}$, which has a radius of 2.6 Å in the dehydrated form. To probe the pore opening capacity of bBest2, we replaced Cl$^-$ in the external solution with CH$_3$SO$_3^-$. Substantial outward CH$_3$SO$_3^-$ current was recorded even in the absence of Ca^{2+}, and was significantly enhanced by 1.2 μM [Ca^{2+}]$_i$ (Fig. 5a–b), indicating that both the neck and aperture in bBest2 (radii = 1.1 Å and 2.2 Å, respectively, Fig. 1d–e) must be dilated to a miminum radius of 2.6 Å upon either spontaneous or Ca^{2+}-dependent channel opening. Moreover, the relative permeability of CH$_3$SO$_3^-$ in bBest2 was right-shifted (Fig. 5b), indicating that CH$_3$SO$_3^-$ is less permeable than Cl$^-$ (Fig. 3d).

To examine the gating of CH$_3$SO$_3^-$, we examined the bBest2 3A and K208A mutants with CH$_3$SO$_3^-$ in the external solution. Remarkably, 1.2 μM [Ca^{2+}]$_i$ significantly stimulated CH$_3$SO$_3^-$ currents from the 3A mutant, but not from the K208A mutant (Fig. 5c–e), suggesting that only the aperture but not the neck is a Ca^{2+}-dependent gate for CH$_3$SO$_3^-$ (Extended Data Fig. 8b). This is in sharp contrast to the case of Cl$^-$, where only the neck but not the aperture serves as a Ca^{2+}-dependent gate (Extended Data Fig. 8a).

Then, how can the neck serve as a gate for Cl^-, but not the bigger $CH_3SO_3^-$? We reasoned that this may reflect a "*trans*" promotive effect of $CH_3SO_3^-$ on the neck, which was illustrated by the increased Cl^- efflux upon the addition of $CH_3SO_3^-$ in the external solution and was previously observed in hBest1[31]. Indeed, replacing Cl^- in the external solution with $CH_3SO_3^-$ resulted in a strong increase of not only outward current ($CH_3SO_3^-$ influx) but also inward current (Cl^- efflux) in WT bBest2, indicating that $CH_3SO_3^-$ on the external side of the channel promotes Cl^- outward movement from the intracellular side in *trans* (Fig. 5b and 5f). Consistent with the results from hBest1[31], the $CH_3SO_3^-$-promoted *trans* effect was abolished in the bBest2 3A mutant, but retained in the K208A mutant (Fig. 5f). Moreover, substantial $CH_3SO_3^-$ currents, but not Cl^- currents, were recorded with the aperture deficient bBest2 K208A mutant in the absence of Ca^{2+} (Fig. 4b and 5c). These results strongly suggest that $CH_3SO_3^-$ promotes opening of the neck (Extended Data Fig. 8b).

Both the aperture and neck are Ca^{2+}-dependent gates for I^-

The Ca^{2+}-dependent gating effect of the bBest2 aperture on $CH_3SO_3^-$ but not Cl^- is consistent with our bBest2 structure model, in which the size of the closed aperture (radius 2.2 Å) is bigger than Cl^- (radius 1.8 Å) but smaller than $CH_3SO_3^-$ (radius 2.6 Å). To further investigate the size of the bBest2 aperture, we examined the gating of I^-, which has a bigger radius (2.2 Å) and better permeability than Cl^- (Fig. 3c–d). When Cl^- in the external solution was replaced with I^-, 1.2 μM $[Ca^{2+}]_i$ significantly stimulated I^- currents from not only WT bBest2, but also from the K208A and 3A mutants (Fig. 6a–d), suggesting that both the neck and aperture are Ca^{2+}-dependent gates for I^-. Consistent with this idea, I^- currents from the 3A and K208A mutants are substantially bigger than those from WT bBest2, both in the absence and presence of Ca^{2+} (Fig. 6d). Notably, only the outward currents (reflecting I^- influx), but not the inward currents (reflecting Cl^- efflux), from the neck-deficient 3A mutant were stimulated by Ca^{2+} (Fig. 6b), reaffirming that the aperture of bBest2 is a Ca^{2+}-dependent gate for I^- but not for Cl^- (Extended Data Fig. 8).

Critical residues for anion selectivity

To investigate the contributions of the neck and aperture to bBest2 ion selectivity (Fig. 7a), we examined bBest2 K208A and 3A mutants by patch clamp with different external solutions. The K208A and 3A mutants exhibited decreased relative permeability for I^- and SCN^-, respectively, but the permeability for other anions remained unaltered (Fig. 7b–e and Extended Data Fig. 6h). This is in sharp contrast to the results from cBest1, where anion selectivity was completely eliminated by alanine substitution at the aperture (V205A), but intact in the 3A mutant[24].

Our bBest2 model predicts that K265 and H91, which are specifically conserved in Best2, may contribute to the channel activity and ion selectivity. K265 is located at the extracellular entrance of the bBest2 transmembrane pore, forming a local narrow point that is absent from the cBest1 and KpBest structures (Fig. 7a). The local resolution at the extracellular entrance to the channel is relatively poor compared to the rest of the channel (Extended Data Fig. 1), suggesting that K265 is dynamically flexible. H91 is located right below the neck with side chains pointing to the ion conducting pathway (Fig. 1d and 7a). To examine the role(s) of K265 and H91 in ion selectivity, we generated the respective alanine substitution mutants,

K265A and H91A, which expressed at similar levels on the cell membrane as the WT (Extended Data Fig. 7). When examined by patch clamp, both K265A and H91A mutants displayed significantly decreased selectivity for SCN^-, while the K265A mutant also exhibited reduced selectivity for I^- (Fig. 7f–i and Extended Data Fig. 6h). These results suggest a critical involvement of both K265 and H91 in bBest2 ion selectivity. In contrast, an alanine substitution outside of the pore region, G199A, did not affect the ion selectivity of the channel (Extended Data Fig. 6h).

Discussion

Here, we solved high-resolution structures of Best2 with the bovine homolog bBest2 under three Ca^{2+} conditions. Overall, a high level of similarity is seen between the Best2 and previously documented Best1 structures, including the Ca^{2+}-binding clasp and flower vase shaped ion conducting pathway. On the other hand, the bBest2 structure also shows unique features at the aperture, highlighted by the K208-E212 salt bridge and K208 with anion bound, and additional narrow points formed by K265 and H91 in the ion conducting pathway. Structure-inspired functional analyses reveal that the aperture in bBest2 is a Ca^{2+}-dependent and size-selective gate, while all restrictions in the ion conducting pathway, including the neck, aperture, and newly identified K265 and H91, are involved in ion selectivity.

The neck and aperture are the two main structural restrictions in the channel ion conducting pathway previously identified in the bacterial and chicken Best1 homologs[22,23]. Now our bBest2 model has extended this structural conservation to the Best2 paralog and to mammals in general. Functionally, the neck and aperture play critical roles in Ca^{2+}-dependent gating and ion selectivity of Best1[23,24,31,32]. Our results indicate that these designated functionalities are conserved in Best2. However, unlike its counterpart in hBest1, the aperture of bBest2 is a Ca^{2+}-dependent gate only for large anions such as I^- and $CH_3SO_3^-$, but not for the relatively smaller Cl^- (Fig. 4–6 and Extended Data Fig. 8). As a result, in the absence of Ca^{2+} bBest2 is conductive for Cl^-, but not for I^- (Fig. 4, Fig. 6 and Extended Data Fig. 8). This size-selective feature fits well with the bBest2 structure, in which the opening of the "closed" aperture (radius 2.2 Å) is apparently bigger than a dehydrated Cl^- (1.8 Å). Consistent with this idea, a bound ion density is present in the aperture of all bBest2 cryo-EM maps (Extended Data Fig. 9), irrespective of Ca^{2+}, potentially representing a Cl^- (present in the cryo-EM sample buffer) passing through the "closed" aperture.

The Ca^{2+}-independent channel activity for Cl^- raises the important question about the substrate anion(s) of bBest2 *in vivo*. Although Best2 was originally identified as a Cl^- channel, compelling evidence suggests that it mediates transport of HCO_3^-, which is bigger than Cl^- (radius 2.2–2.3 Å vs. 1.8 Å), in colonic goblet cells and sweat glands[20,21]. Moreover, Best2 is expressed in the basolateral plasma membrane of NPE cells, where it regulates IOP[15,16]. As an anion channel, Best2 could regulate IOP directly by mediating Cl^- transport, which has been suggested to be the rate-limiting factor of aqueous humor formation in the eye[33,34], or indirectly by mediating HCO_3^- transport, which affects intracellular and intraocular pH. The permeability and conductance of HCO_3^- in hBest1, hBest2 and mBest2 were previously documented after heterologous expression: all three

channels are highly permeable to HCO_3^- (P_{HCO3}/P_{Cl} ~0.44 for hBest1, and 0.6–0.7 for hBest2 and mBest2), and have similar conductance for HCO_3^- and Cl^- ($G_{HCO3}/G_{Cl} = 0.9 – 1.1$)[35]. However, the physiological role of Best2 in conducting Cl^- or HCO_3^- in NPE cells has not been directly demonstrated.

Previous studies suggested that the aperture (V205) in cBest1 (radius 1.3 Å) does not contribute to the Ca^{2+}-dependent gating of Cl^-, and a Ca^{2+}-independent "breathing" mechanism was proposed[22]. Our results suggest that Ca^{2+}-dependent activation of the aperture is at play for large ions including I^- and $CH_3SO_3^-$, even in bBest2 whose aperture has a much bigger opening than that of cBest1 (radius 2.2 Å vs. 1.3 Å). Therefore, we suspect that the aperture in cBest1 is a Ca^{2+}-dependent gate for bigger halides such as Br^- and I^-. Although the hBest1 structure has not been solved, the presence of a bulky isoleucine at the aperture (I205) predicts a small opening in the closed state, potentially similar to its counterpart in KpBest (I180, radius 0.9 Å). Supporting this idea, the hBest1 aperture is a Ca^{2+}-dependent gate for Cl^-[31]. We propose that Ca^{2+}-binding triggers the dilation of the aperture in all mammalian bestrophins, but Ca^{2+}-dependent gating is only effective when the size of the passing anion is bigger than the closed aperture after taking "breathing" into account (Extended Data Fig. 8).

On the other hand, the role of the neck as a major Ca^{2+}-dependent gate appears to be clear and conserved among all examined Best1 and Best2 homologs[24,31,32]. Notably, the neck serves as a gate for Cl^-, Br^- and I^-, but not for the bigger $CH_3SO_3^-$ due to a *trans* promotive effect: the addition of $CH_3SO_3^-$ in the external solution enhances not only the influx of $CH_3SO_3^-$, but also the efflux of Cl^-. This *trans* effect was observed in the WT and aperture alanine substitution mutant (K208A), but not in the neck alanine substitution mutant (3A), suggesting that the neck, but not the aperture, is activated by $CH_3SO_3^-$. Notably, *trans* effect has been documented for Ca^{2+}-activated Cl^- channels[27,36], and is suggested to reflect the influence of the ion, $CH_3SO_3^-$ in this case, on channel gating (Extended Data Fig. 8)[31].

Interestingly, although SCN^- has a similar size as I^-, Best2-mediated SCN^- currents were much smaller than I^- currents at the same $[Ca^{2+}]_i$. This observation may be attributed to SCN^- sticking to the channel, which depends on a conserved S79[26–28]. Consistent with this idea, a recent study described a cBest1 structure in which the pore-lining helix at the neck rotates upon activation[32], moving F80 away from the pore, widening the constriction and exposing S79 to the solvent within the transmembrane pore.

In our ion selectivity experiments, Na^+ was used as the cation in all patch solutions, and was taken into account when P_x/P_{Cl} (X = CH_3SO_3, Br, I or SCN) was calculated. As $CH_3SO_3^-$ is the least permeable ion among all those tested in this study, the existence of permeable Na^+ in the patch solution would theoretically have the most interference on the calculated P_{CH3SO3}/P_{Cl}. To test this possibility, we used impermeable $NMDG^+$ as the cation to re-examine P_{CH3SO3}/P_{Cl}. The resultant P_{CH3SO3}/P_{Cl} values from both approaches were consistent (Extended Data Fig. 6g), validating our ion selectivity results. However, it should be noted that using impermeable $NMDG^+$ as the cation is a more stringent condition for ion selectivity experiments.

The neck and aperture are structural landmarks in all three available high-resolution bestrophin models, solved from KpBest, cBest1 and bBest2. Notably, a higher level of conservation is seen at the neck, which consists of three hydrophobic I or F residues in these species, as compared to the aperture, which changes from a hydrophobic I or V in KpBest/ cBest1 to a positively charged K in bBest2. Further sequence alignment with more vertebrate bestrophin homologs reveals a unique composition of the Best2 aperture (Supplementary Fig. 3): 1) the neck forming residues I76, F80 and F84 are perfectly conserved in all examined vertebrate bestrophins; 2) among the four paralogs, only Best2 does not have a hydrophobic I or V at the 205 position; 3) all examined vertebrate Best2 homologs have a positively charged K208 and a negatively charged E212, which are connected through a salt bridge and form the aperture in bBest2. Taken together, we predict that Best3 and Best4 both have a hydrophobic I or V aperture mirroring that of Best1, while the unique aperture of Best2 underlies distinct functionality of the channel, such as Ca^{2+}-independent activity, compared to the other three paralogs.

Previous studies indicate important involvement of the neck and aperture in Ca^{2+}-dependent gating and anion selectivity; however, a consensus has not been established. A clear separation of function was reported with cBest1, where Ca^{2+}-dependent gating and anion selectivity are solely controlled by the neck and aperture, respectively[24]. By contrast, studies from other species suggest the involvement of both constrictions in these functionalities[23,31]. Our results from bBest2 support the latter scenario (Fig. 4–7).

Methods

Cell lines

HEK293 cells authenticated by short tandem repeat DNA profiling were kindly gifted from Dr. David Yule at University of Rochester. DMEM (4.5 g L^{-1} glucose, Corning 10013CV) supplemented with 10% FBS and 100 μg ml^{-1} penicillin-streptomycin was used for HEK293 cell culture. No mycoplasma contamination was found by DAPI staining.

Transfection

20–24 hours before transfection, HEK293 cells were detached by treatment with 0.25% trypsin for 5 minutes at room temperature and split into new 3.5-cm culture dishes at 50% confluency. PolyJet transfection reagent (SignaGen SL100688) was used to transfect HEK293 cells with plasmids bearing the indicated WT or mutant channels (1 μg). The transfection mix was removed after 6–8 hours, and cells were washed with PBS and cultured in supplemented DMEM. 24 hours after transfection, cells were detached by trypsin and split onto fibronectin-coated glass coverslips for patch clamp[27].

Immunoblotting

HEK293 cells transiently expressing CFP tagged bBest2 WT and mutant channels were harvested 48 hours post transfection. The M-PER Mammalian Protein Extraction Reagent (Thermo Fisher Scientific 78501) and Mem-PER Plus Membrane Protein Extraction Kit (Thermo Fisher Scientific 89842) were used to prepare the total cell lysates and membrane-associated proteins, respectively. The samples were mixed with Laemmli buffer and

denatured at 95°C for 5 minutes, followed by SDS-PAGE and wet transfer to nitrocellulose membranes. Immunoblotting was performed with GFP primary antibody (1:1,000, Thermo Fisher Scientific A-6455) and fluorophore-conjugated secondary antibody (1:10,000, LI-COR Biosciences 926–68071), and subsequently detected by infrared imaging. β-actin loading control was detected by a monoclonal primary antibody (1:1,000, Thermo Fisher Scientific MA5–15739) and HRP-conjugated secondary antibody (1:10,000, Thermo Fisher Scientific 04–6020), followed by ECL.

Electrophysiology

Electrophysiological analyses were conducted 72–96 hours after transfection. Whole-cell patch clamp recording was performed with an EPC10 patch clamp amplifier (HEKA Electronics) controlled by Patchmaster (HEKA). Micropipettes were pulled and fashioned from filamented 1.5 mm thin-walled glass (WPI Instruments), and filled with internal solution containing (in mM): 130 CsCl, 1 $MgCl_2$, 10 EGTA, 10 HEPES (pH 7.4, adjusted by CsOH) for Fig. 2 and Figs. 4–6. The desired free Ca^{2+} concentration was obtained by adding $CaCl_2$ (maxchelator.stanford.edu/CaMgATPEGTA-TS.htm). Series resistance was typically 1.5–2.5 MΩ, with no electronic series resistance compensation. The recipe of external solution was (in mM): 140 NaCl, 5 KCl, 2 $CaCl_2$, 1 $MgCl_2$, 10 HEPES (pH 7.4, adjusted by NaOH) and 15 glucose for Figs. 2 and 4. For Ca^{2+}-dependent conductance measurement with different anions, when replacing Cl^- with X (X = I^- or $CH_3SO_3^-$) in Figs. 5–6, the external solution was 120 NaX and 10 HEPES (pH 7.4, adjusted by NaOH). For ion selectivity experiments, when replacing Cl^- with X (X = Br^-, I^-, SCN^- or $CH_3SO_3^-$) in Figs. 3 and 7, the internal solution was 120 NaCl, 0.21 EGTA, 10 HEPES (pH 7.4, adjusted by NaOH). The desired free Ca^{2+} concentration (1.2 μM) was obtained by adding $CaCl_2$. The external solution was 120 NaX and 10 HEPES (pH 7.4, adjusted by NaOH). When measuring the relative Na^+ to Cl^- permeability, the external solution was 30 NaCl and 10 HEPES (pH 7.4, adjusted by NaOH). In control experiments, both the internal and external solutions (pH 7.4) were adjusted by NMDG in Extended Data Fig. 6f; 120 NMDG-Cl and NMDG-CH_3SO_3 instead of NaCl and NaCH$_3$SO$_3$ were added in the internal and external solutions, respectively, in Extended Data Fig. 6g. Solution osmolarity was 290~310 mOsm/L with glucose, and ~5 mOsm lower in the internal solutions than the external solutions of the same experiment. The low and high Ca^{2+} solutions in the same set of experiments were adjusted to have the exact same osmolarity.

Traces were acquired at a repetition interval of 4 s[28]. Currents were sampled at 25 kHz and filtered at 5 or 10 kHz. I-V curves were generated from a group of step potentials (−100 to +100 mV from a holding potential of 0 mV). Experiments were conducted at room temperature (23 ± 2 °C). Liquid junction potentials were measured and corrected using HEKA built-in functions. Solution changes were performed manually.

Molecular cloning

All constructs were made by site-directed mutagenesis PCR with the In-fusion Cloning Kit (Clontech) and verified by sequencing.

Protein production and purification

HEK293-F cells were gifted from Dr. Ravi Kalathur. To produce $bBest2_{1-406}$, HEK293-F cells were infected with BacMam baculoviruses bearing $bBest2_{1-406}$ (MOI = 5), and cultured at 37 °C for 72–96 hours before harvesting[37]. 10 mM sodium butyrate was added to HEK293-F culture 24 hours post infection.

Cells were harvested by centrifugation at 200 g in 4°C and stored at −80°C until use. Cell pellets were resuspended in a buffer containing 50 mM HEPES (pH 7.8), 300 mM NaCl, 5% glycerol, 20 mM imidazole, 1 mM PMSF, EDTA-free protease inhibitor cocktail (Sigma S8830), and 0.5 mM TCEP, and lysed using an emulsiflex-C3 high pressure homogenizer (Avestin). The cell lysate was incubated with a final concentration of 2% (w/v) n-Dodecyl β-D-maltopyranoside (DDM) (Anatrace) for 1 hour at 20°C with gentle rocking. The non-dissolved content was pelleted by ultracentrifugation at 150,000 g in 4°C for 30 min. The supernatant was carefully collected and loaded to a pre-equilibrated 5 mL HisTrap Ni^{2+}-NTA affinity column (GE Healthcare). After 13 column-volume buffer wash, the protein was eluted with a buffer containing 25 mM HEPES (pH 7.8), 200 mM NaCl, 5% glycerol, 500 mM imidazole, 0.1 mM TCEP and 0.05% (w/v) DDM. The resulting samples were concentrated with 100 kDa centrifugal filter units (Amicon Ultra-15, Millipore) to a final volume of 400–500 μL for size-exclusion chromatography with a Superdex-200 column by HPLC (AKTA pure 25, GE Healthcare). The desired free Ca^{2+} concentration was obtained by adding $CaCl_2$ and EGTA (maxchelator.stanford.edu/CaMgATPEGTA-TS.htm).

Cryo-EM sample preparation

For the EGTA and 5 mM Ca^{2+} datasets, bBest2 was purified as previously described with a few modifications. After nickel elution in DDM, imidazole was removed by buffer exchange on a 15mL concentrator. TEV protease was added for 2–5 hours and the cleaved GFP with 10x his tag and TEV (with 6x his tag) was removed by incubation with nickel slurry. bBest2 left in the flow through was concentrated to 3 mg mL^{-1} and amphipol PMAL-C8 (Anatrace) was added at a protein:amphipol mass ratio of 1:4. After 1–3 hours incubation with PMAL-C8 rocking at 4 °C, activated SM-2 Bio-Beads (Bio-Rad) were added and incubated rocking overnight to remove detergent. On the next morning, fresh Bio-Beads were added for about 30 minutes to ensure the complete removal of detergent and the protein was injected onto a Superdex-200 in gel filtration buffer lacking detergent (200 mM NaCl, 40 mM HEPES, 0.1 mM TCEP, pH 7.8). The peak corresponding to pentameric bBest2 was concentrated for grid preparation (Vivaspin 500, 100,000 MWCO PES, sartorius). Grids were prepared with protein at 0.5–0.8 mg mL^{-1} in gel filtration buffer. As bBest2 exhibits preferred orientation (top views only) in both amphipols tested (A8–35 and PMAL-C8) and in nanodisc, various additives were tested for the ability to improve the angular distribution and it was determined that addition of 0.1–0.2 % PMAL-C8 to the protein directly prior to vitrification resulted in excellent particle distribution and an abundance of side views, allowing 3D reconstruction. 3 μL of protein was mixed with appropriate stock solutions to generate final concentrations of 5 mM $CaCl_2$ or 20 mM EGTA, followed by addition of PMAL-C8 to a final concentration of 0.1–0.2 %. 3 μL of the protein mixture was added to plasma-treated UltrAuFoil R0.6/1 holey gold grid (EMS) at 12 °C and 100% humidity, incubated for 10–15 s, and then blotted for 6–12 s and plunged into liquid ethane cooled by liquid nitrogen with a

Vitrobot Mark IV. For the EGTA state, care was taken to use calcium-free filter paper (Whatman quantitative ashless filter paper Grade #40, WHA1440150) and Whatman #1 was used for the high Ca^{2+} state. In all cases, two filter papers were used on the right side of the Vitrobot arm (same side as protein addition) with one paper on the left, which reduced the blotting time.

For the 250 nM Ca^{2+} dataset, pure protein in DDM was transferred to amphipol A8–35 (Anatrace) for 4 hours with gentle agitation at 4 °C, followed by overnight incubation with SM-2 Bio-Beads (Bio-Rad) to remove the detergent. On the next day, the protein in A8–35 was further purified by a final round of size exclusion chromatography with a Superdex-200 column in the absence of detergent. The peak corresponding to pentameric bBest2 was concentrated to 0.5–0.8 mg mL^{-1} and 2.8 μL was applied to a plasma-treated UltrAuFoil R0.6/1 holey gold grid (EMS) using a Vitrobot Mark IV (ThermoFisher) after addition of appropriate EGTA and Ca^{2+} mixture. The initial sample in A8–35 exhibited highly preferred orientation (top views only) and addition of 0.06 mM DDM to the protein-amphipol complex immediately prior to grid application was found to fix the issue.

Cryo-EM data collection

All datasets were collected on a Titan Krios (Thermo-Fisher) with K2 or K3 direct electron detector (Gatan) using Leginon for automated data collection[38].

The 20 mM EGTA state was imaged on "Krios1" at the Simons Electron Microscopy Center, a part of the New York Structural Biology Center. 4,314 movies were collected on the K2 direct electron detector (Gatan) at 22,500x mag, corresponding to a physical pixel size of 1.07 Å/pix, with a total dose of 69.67 e^{-}/Å^2 and a nominal defocus range of 0.8 to 1.5 μm. Ice thickness was monitored as previously described and targets were chosen in ice ranging in thickness from 20 to 100 nm[39].

The 5 mM Ca^{2+} state was imaged on "Krios Z" at Columbia University, which is equipped with a K3 direct electron detector (Gatan) and energy filter. 5,700 movies were collected at 105,000x mag, corresponding to a physical pixel size of 0.83 Å/pix, with a total dose of 58 e^{-}/Å^2 and a nominal defocus range from 0.8 to 1.4 μm.

The 250 nM Ca^{2+} state was imaged on "Krios 1" at the Simons Electron Microscopy Center, a part of the New York Structural Biology Center. 6,781 movies were collected on the K2 direct electron detector (Gatan) at 29,000x mag, corresponding to a physical pixel size of 0.83 Å/pix with a total dose of 73.14 e^{-}/Å^2 and a nominal defocus range from 1.50 to 2.50 μm.

Cryo-EM image processing

EGTA dataset movies were imported to cryoSPARC2 (v2.12.4) for processing. Movies were aligned using patch motion correction, followed by CTF estimation by Patch CTF. Templates were generated by blob-based autopicking on a small subset of micrographs. These particles underwent a few rounds of 2D classification to generate clean 2D classes for template-based autopicking, which resulted in picking 3,714,156 particles from 4,314 micrographs. Particles underwent multiple rounds of 2D classification with binning to

remove "bad" particles, consisting of particles that may be from thick ice, damaged, adhered and denatured at the air-water interface, and those which may not correspond to protein at all (ice, gold, etc). From initial 2D classification, 935,352 particles were selected for further 3D classification at a pixel size of ~1.67 Å/pix. Particles underwent *ab initio* reconstruction and homogeneous refinement to 3.43 Å, followed by heterogeneous refinement into four classes. One class exhibited excellent features while the other three displayed artifacts or non-continuous helices. The good class, consisting of 562,619 particles underwent homogeneous refinement and particles were extracted without binning. The particles were extracted with a box size of 200 pixels and underwent *ab initio* reconstruction followed by homogeneous refinement to 2.24 Å. Heterogeneous refinement into four classes revealed one class with excellent features and semi-ordered N-terminal extension (Class #4, 287,708 particles) and another class with disordered N-terminal extension (Class #2, 124,043 particles). The class with ordered N-terminal extension underwent homogeneous refinement to 2.31 Å, followed by local motion correction in cryoSPARC2 (2.12.4) using a box size of 256 pixels. Particles underwent *ab inito* reconstruction and "Refinement NEW" with per-particle defocus optimiation and per-group CTF optimization (tilt, trefoil, spherical aberration, and tetrafoil) to 2.19 Å, followed by Non-uniform refinement to 2.19 Å. Particles were symmetry expanded and underwent local refinement (with Non-Uniform Refinement, lowpass 8 Å) using the same refinement mask from Non-uniform refinement, resulting in a map at overall 2.17 Å resolution. This map underwent density modification in Phenix (ResolveCryoEM, phenix-dev-3699) and was resampled on a finer grid using new Cryo-EM tools (Sharpen/ Blur Map) in Coot 0.9-pre with a sharpening factor of −2 and resample factor of 3.0, resulting in a map with final voxel size of 0.35 Å^2/vox[40]. The map with disordered N-terminal extension was processed in a similar manner. 124,043 particles from heterogeneous refinement underwent homogeneous refinement to 2.55 Å. Particles underwent local motion correction in cryoSPARC2 (2.12.4) using a box size of 256 pixels, followed by *ab initio* reconstruction and "Refinement NEW" with per-particle defocus optimiation and per-group CTF optimization (tilt, trefoil, spherical aberration, and tetrafoil) to 2.36 Å, followed by Non-Uniform refinement to 2.36 Å. Particles were symmetry expanded and underwent local refinement (with Non-Uniform Refinement, lowpass 8 Å) using the same refinement mask from Non-Uniform refinement, resulting in a map at overall 2.33 Å resolution. The map was filtered according to local resolution from blocres as implemented in cryoSPARC2 (2.12.4) and was resampled on a finer grid in Coot with a sharpening factor of −2 and resample factor of 3.0.[57]

High Ca^{2+} dataset movies were imported to cryoSPARC2 (v2.12.4) for processing. 5,700 movies were aligned using patch motion correction, followed by CTF estimation by Patch CTF. Nearly 2,000 micrographs were overfocused, likely due to deformation of the grid and inaccurate z-focusing. Only the micrographs with estimated resolution 3.5 Å or better were kept for further processing and overfocused images were removed, leaving 3,418 good micrographs. Templates were generated by blob-based autopicking on a small subset of micrographs and these particles underwent a few rounds of 2D classification to generate clean 2D classes for template-based autopicking, which resulted in picking 3,734,960 particles from 3,418 micrographs. Particles were extracted with binning and underwent multiple rounds of 2D classification to remove "bad" particles. From initial 2D

classification, 1,737,124 particles were selected for further 3D classification at a pixel size of ~1.43 Å/pix. These particles underwent *ab initio* reconstruction, followed by heterogeneous refinement into 6 classes. The three best classes were combined for homogeneous refinement to 2.93 Å. Particles were extracted without binning at the original pixel size of 0.83 Å/pix and underwent *ab initio* reconstruction, followed by "Refinement NEW" with per-particle defocus optimization to 2.85 Å. Particles underwent local motion correction (per-particle motion correction) with a box size of 340 pixels, followed by *ab initio* reconstruction and "Refinement NEW" with per-particle defocus optimization and per-group CTF parameter optimization for tilt, trefoil, spherical aberration, and tetrafoil, which refined to 2.39 Å. Heterogeneous refinement was performed and the class with best features and highest number of particles was chosen for the final homogeneous refinement to 2.36 Å. This map underwent density modification in Phenix (ResolveCryoEM, phenix-dev-3699) and was resampled on a finer grid using new Cryo-EM tools (Sharpen/Blur Map) in Coot 0.9-pre with a sharpening factor of −2 and resampling factor of 2.0 and, resulting in final voxel size of 0.41 Å^2/vox[40]

For the 250 nM Ca^{2+} state, frame alignment and dose-weighting were performed using UCSF MotionCor2 in 5×5 patches[41]. CTF was estimated with gCTF on non-dose-weighted micrographs[42]. Automated particle picking was performed in Relion using 2D class templates obtained from manually picked particles[43]. Particles were binned to 4 Å/pix during extraction and imported to cryoSPARC for initial 2D classification[44]. Multiple rounds of 2D classification were performed to remove bad particles, such as ice, detergent, gold and low-resolution protein particles from thick ice. 3D *ab initio* reconstruction was performed, followed by homogeneous refinement with C5 symmetry. Particles were then re-centered and extracted in Relion without binning with a final pixel size of 0.83 Å/pix. Particles were then imported to cryoSPARC v2 (2.11) for further processing. Unbinned particles underwent one round of 2D classification, followed by 3D *ab initio* reconstruction, heterogeneous refinement, homogeneous refinement, and non-uniform refinement. Initial reconstructions processed with C1 symmetry exhibited C5 symmetry and subsequent processing was carried out with C5 symmetry enforced. Heterogeneous refinement into four classes was performed on the initial *ab initio* reconstruction, resulting in one "good" class which could be refined to high resolution and had densities for each helix, as well as three "bad" classes, which could not be further refined beyond 8 Å and which lacked densities for expected helices. The good class consisted of 33,348 particles and was refined to 3.00 Å with homogeneous refinement. The resulting maps had strong densities for residues 24 to 340, while the N- and C-termini had weak density, indicating possible heterogeneity in this region. Heterogeneous refinement into two classes resulted in one class with strong density for the N-terminus, moderate density for the C-terminus, and good density for residues 301–304 of the acidic Ca^{2+}-clasp (consisting of 18,972 particles), as well as one class which lacked these densities (consisting of 14,376 particles). The class with strong densities for the N- and C-termini, and Ca^{2+}-clasp underwent homogeneous refinement to 3.08 Å, followed by non-uniform refinement to 3.04 Å. The class with disordered N-terminus and C-terminus underwent homogeneous refinement to 3.27 Å, followed by non-uniform refinement to 3.11 Å. The particles were transferred to Relion with the aid of pyem, reconstructed using Relion_reconstruct, post-processed, and underwent CTF refinement (per-particle

defocus)[45,46]. CTFrefined particles were then imported to cryoSPARC v2 for a final round of non-uniform refinement. The Ca^{2+}-bound class was refined to 3.00 Å, while the Ca^{2+}-unbound class was refined to 3.03 Å. The final Ca^{2+}-bound map was obtained by performing post-processing in Relion3.0, while the final Ca^{2+}-unbound map was obtained by performing local filtering in cryoSPARC v2.

All reported resolutions were computed by cryoSPARC v2 with tight mask using the gold standard Fourier shell correlation (FSC) of 0.143. As further validation, 3DFSC was used to assess the directional anisotropy of the samples and the sphericity was found to be acceptable (>0.9) for each sample.

Model building and refinement

A homology model for bBest2 was generated using the Swiss-Model server from the chicken Best1 crystal structure (PDB 4RDQ)[22,47–51]. Using this homology model as a starting point, real space refinement was performed in Phenix[52], followed by manual adjustment in Coot[53]. Real space refinement was performed iteratively in Coot and Phenix until the final model was generated. Water molecules were added manually in Coot for the three maps with best resolution (high Ca^{2+} map and both maps from the Ca^{2+}-free condition).

The model was validated using comprehensive validation tools in Phenix, including the use of MolProbity to assess geometry constraints[54], phenix.mtriage to compute the map-to-model FSC[55], and EMRinger to assess model fit[56]. Local resolution estimation was performed using the blocres package from Bsoft[57], as implemented in cryoSPARC v2.

All structure figures were generated with PyMOL or UCSF Chimera[58]. HOLE was used to compute the pore dimensions, while Caver3.0 was used to generate pore densities for figures[59].

Electrophysiological data collection and analyses

Whole-cell patch clamp data were processed off-line in Patchmaster. Statistical analyses were performed using built-in functions in Origin. A sufficient number of samples were examined to reach statistical conclusion according to the specific method utilized in that experiment.

The X^- to Cl^- relative permeability (P_X/P_{Cl}) was calculated according to the Goldman-Hodgkin-Katz equation taking P_{Na}/P_{Cl} into account. The relative $CH_3SO_3^-/Cl^-$ (with $CH_3SO_3^-$ or Cl^- in the external solution) inward movement (outward current) conductance ($G_{CH3SO3\ with\ ex-CH3SO3}/G_{Cl\ with\ ex-Cl}$) was measured as slope conductance at the reversal potential plus 50 mV, and $CH_3SO_3^-$ current was multiplied by 1.2 to compensate for the concentration difference. The *trans* effect, representing the relative Cl^- (with $CH_3SO_3^-$ or Cl^- in the external solution) outward movement (inward current) conductance ($G_{Cl\ with\ ex-CH3SO3}/G_{Cl\ with\ ex-Cl}$), was measured as slope conductance at the reversal potential minus 50 mV.

Statistics and Reproducibility

A sufficient number of samples were examined to reach statistical conclusion according to the specific method utilized in that experiment. Statistically significant differences ($P<$ 0.05) between means of two groups were determined by two-tailed Student t test. Data are presented as means ± s.e.m.

Reporting Summary Statement

Further information on experimental design is available in the Nature Research Reporting Summary linked to this article.

Data Availability

Atomic models are available through the Protein Data Bank with accessions codes 6VX5, 6VX6, 6VX7, 6VX8 and 6VX9; cryo-EM reconstructions are available through the EMDB with accession codes EMD-21430, EMD-21431, EMD-21432, EMD-21433 and EMD-21434.

Source data for Figure 2–7 are available with the paper online.

Extended Data
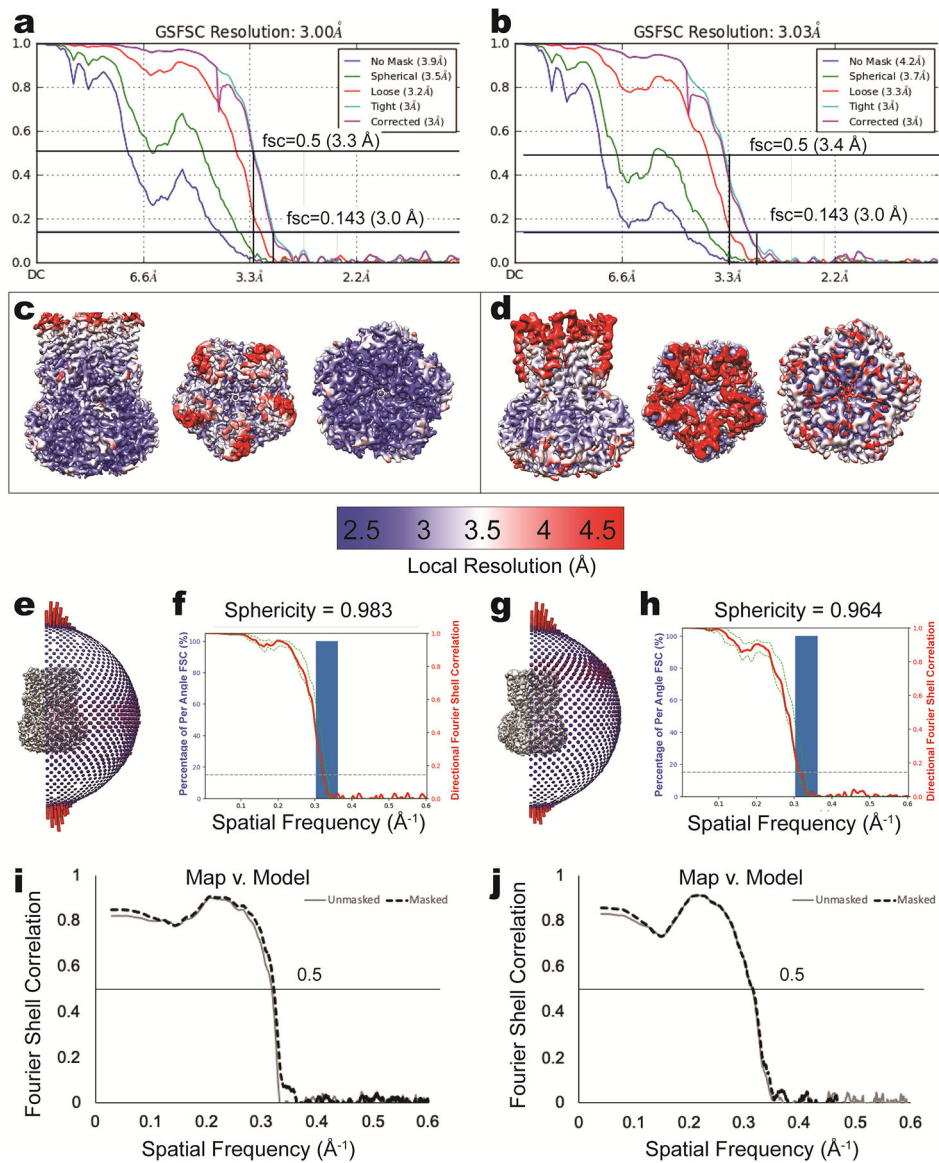
Extended Data Fig. 1. Structure determination of bBest2 with 250 nM Ca^{2+}.
(**a**, **b**) FSC curve for masked and unmasked map generated by cryoSPARC v2 non-uniform refinement for Ca^{2+}-bound (**a**) and Ca^{2+}-unbound (**b**) states. (**c**, **d**) Local resolution estimation calculated by blocres as implemented in cryoSPARC v2 for Ca^{2+}-bound (**c**) and Ca^{2+}-unbound (**d**) states. (**e**) Viewing angles for particles contributing to final map as implemented by pyem star2bild script for Ca^{2+}-bound state. (**f**) Analysis of sphericity of final maps by 3DFSC server to assess directional anisotropy of specimens with slightly preferred orientation for Ca^{2+}-bound state. (**g**, **h**) The same format for the Ca^{2+}-unbound state. Blue histogram indicates percentage of per angle FSC. Red solid line indicates directional FSC and green dashed line indicates +/− 1 standard deviation from mean of directional FSC. (**i**, **j**) Map v. Model FSC curve with and without mask as implemented by Phenix.validation package for Ca^{2+}-bound (**i**) and Ca^{2+}-unbound (**j**) states.
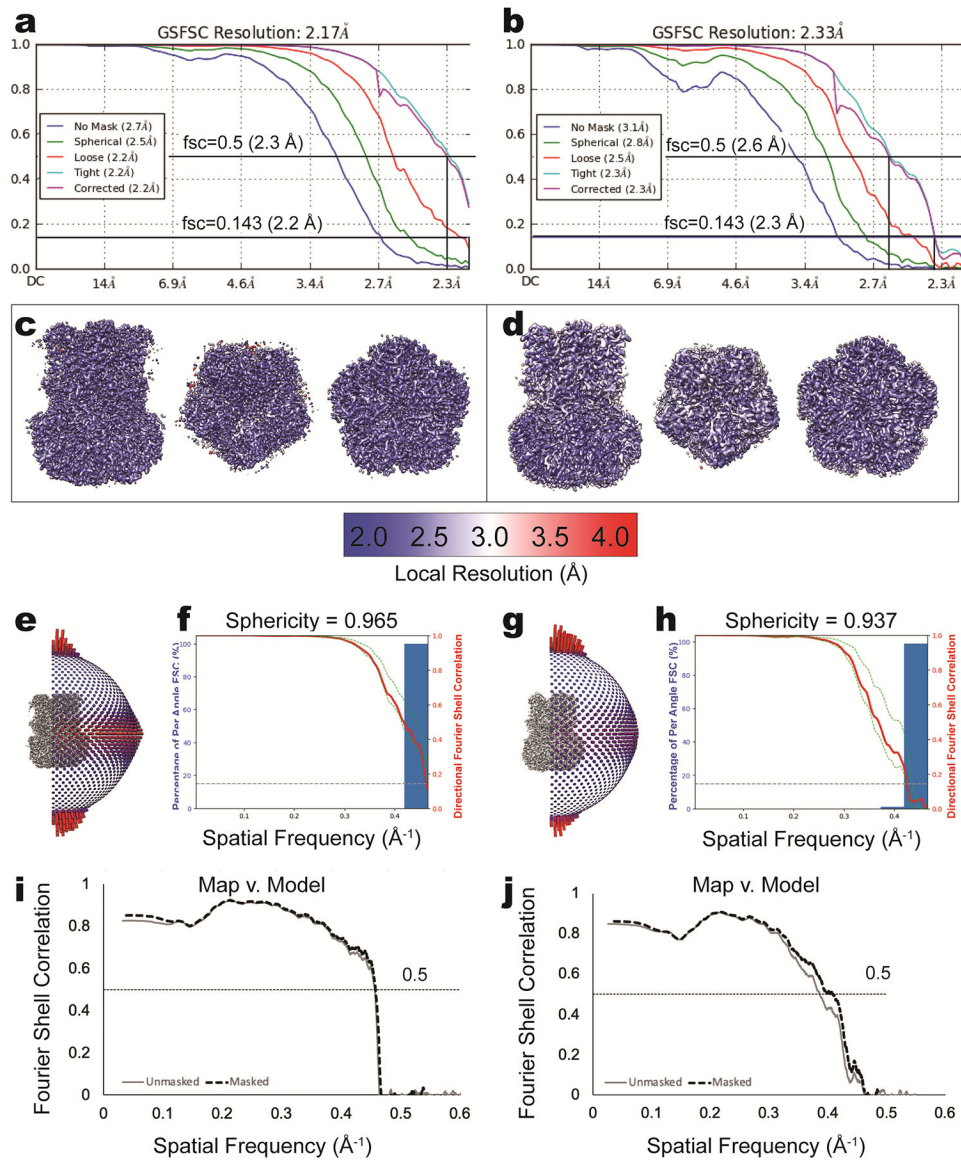
Extended Data Fig. 2. Structure determination of bBest2 with EGTA only.
In the same format as Extended Data Figure 2. *Left* (**a**, **c**, **e**, **f**, **i**), Ca^{2+}-unbound state 1 (N-terminus partially disordered); *right* (**b, d, g, h, j**), Ca^{2+}-unbound state 2 (N-terminus completely disordered).
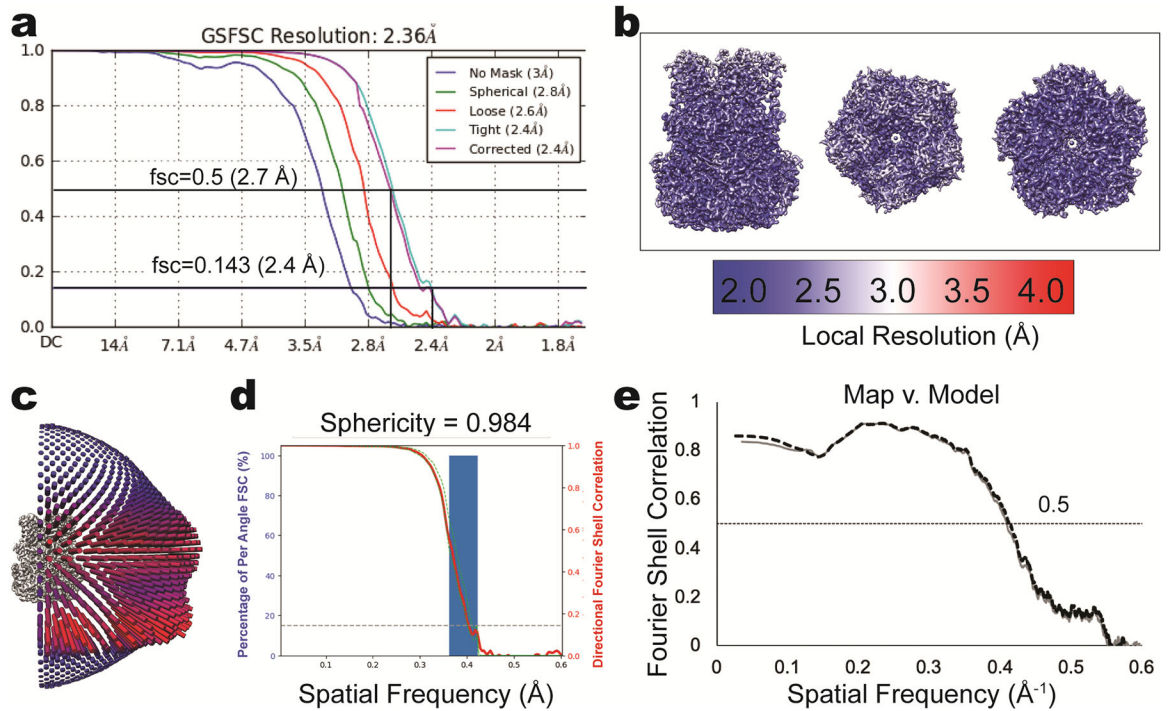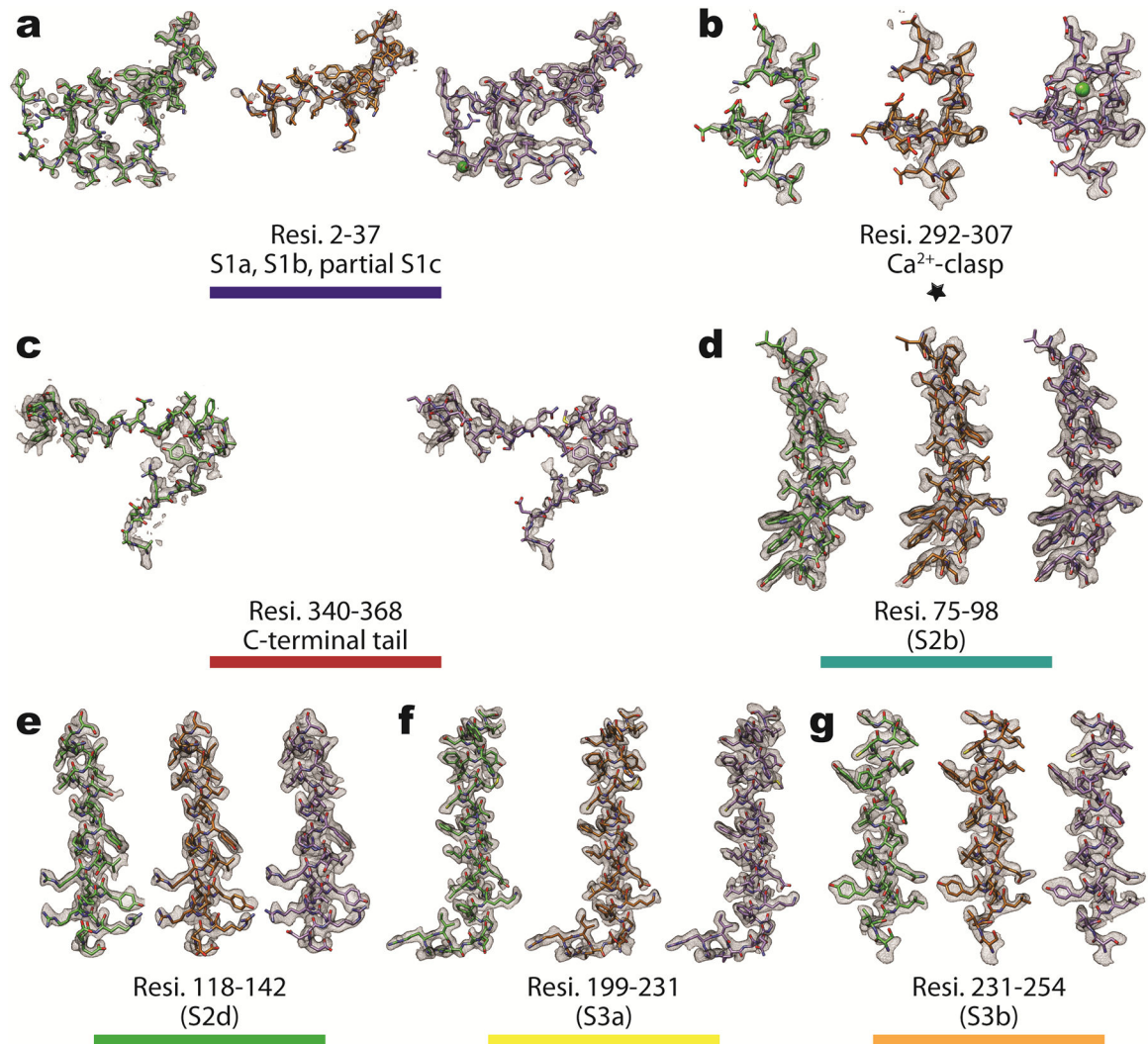
Extended Data Fig. 3. Structure determination of bBest2 with 5 mM Ca²⁺.
In the same format as Extended Data Figure 2 and 3. (**a**) FSC curve generated in cryoSPARC. (**b**) Local resolution from blocres. (**c**) Viewing angles for particles contributing to final map. (**d**) Analysis of sphericity. (**e**) Map v. Model FSC curve with and without mask.
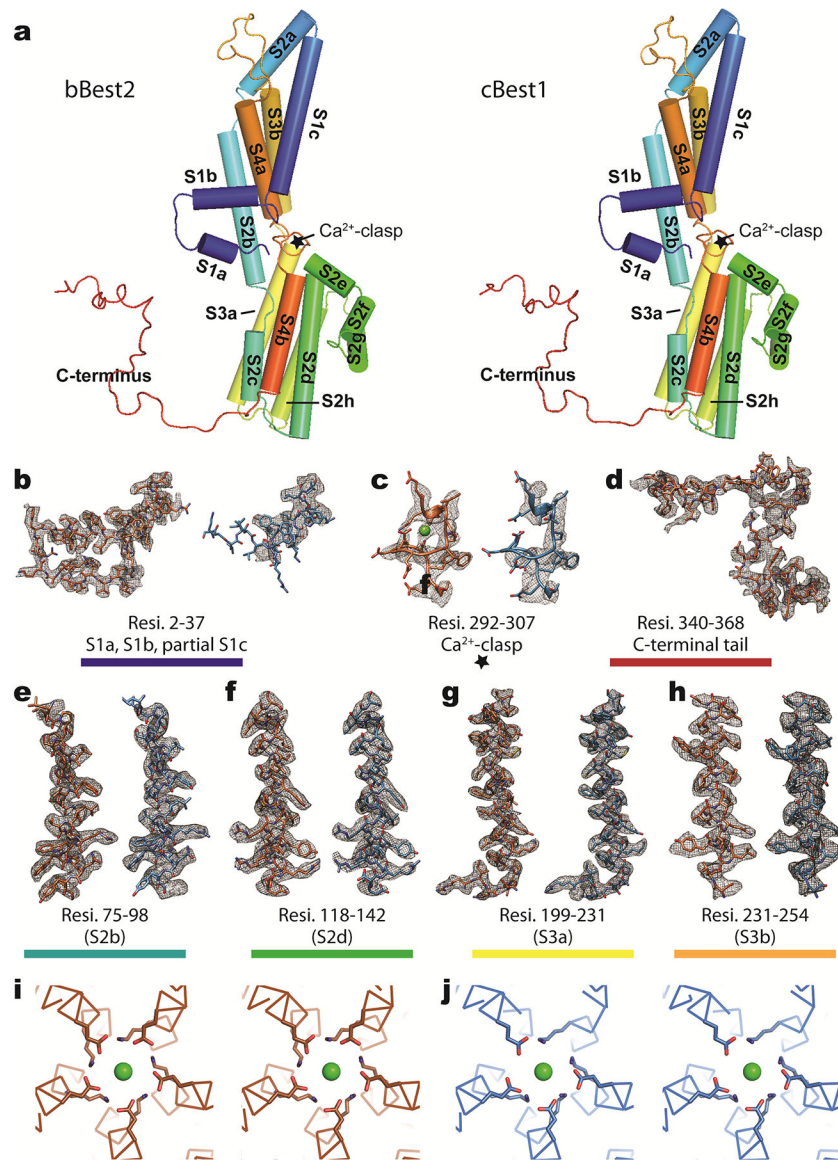
Extended Data Fig. 4. Representative cryo-EM density for the two bBest2 cryo-EM structures with 250 nM Ca²⁺.

(**a**) Architecture of an individual bBest2 protomer (*left*) and cBest1 protomer (4RDQ, *right*), both Ca²⁺-bound and color-coded by segments in accordance with Supplementary Figure 1. (**b-h**) Representative map densities for indicated regions are shown with the corresponding atomic model. The Ca²⁺-bound state (ordered N-terminus) and Ca²⁺-unbound state (completely disordered N-terminus) structures are shown in orange (*left*) and blue (*right*), respectively. Green dot, a Ca²⁺ ion. (**i**, **j**) Stereo images of bBest2, presenting the aperture region for divergent "wall-eyed" viewing. Orange, Ca²⁺-bound (**i**); blue, Ca²⁺-unbound (**j**). Green dot, a Cl⁻ ion.

a Resi. 2-37
S1a, S1b, partial S1c

b Resi. 292-307
Ca²⁺-clasp
★

c Resi. 340-368
C-terminal tail

d Resi. 75-98
(S2b)

e Resi. 118-142
(S2d)

f Resi. 199-231
(S3a)

g Resi. 231-254
(S3b)

Extended Data Fig. 5. Representative cryo-EM density for bBest2 cryo-EM structures with EGTA only and 5 mM Ca²⁺.

(**a-g**) Representative map densities for indicated regions are shown with the corresponding atomic model. The Ca²⁺-unbound state 1 (partially disordered N-terminus, EGTA only), Ca²⁺-unbound state 2 (completely disordered N-terminus, EGTA only) and Ca²⁺-bound state (ordered N-terminus, 5 mM Ca²⁺) structures are shown in green (*left*), pumpkin (*middle*) and purple (*right*), respectively. Green dot, a Ca²⁺ ion.
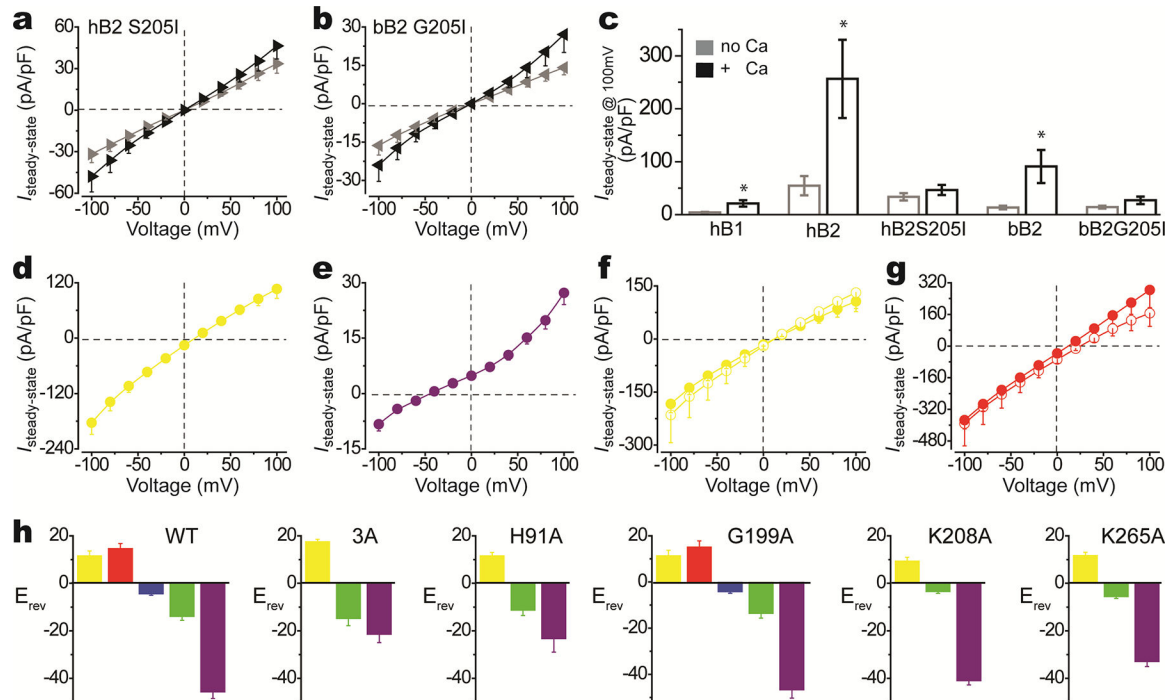
Extended Data Fig. 6. Critical residues in Best1 and Best2.
(**a**, **b**) Population steady-state current density-voltage relationships from HEK293 cells expressing hBest2 S205I (**a**) or bBest2 G205I (**b**) in the absence (gray) and presence (black) of 1.2 μM $[Ca^{2+}]_i$; n= 9–20 for each point. (**c**) Bar chart showing the steady-state current densities from HEK293 cells expressing the indicated Best1 and Best2 channels in the absence (gray) and presence (black) of 1.2 μM $[Ca^{2+}]_i$, n= 5–20 for each bar. *$P < 0.05$ compared to currents without Ca^{2+} under the same condition, using two-tailed unpaired Student t test. (**d**, **e**) Population steady-state current density-voltage relationships from HEK293 cells expressing WT bBest2 in the presence of 1.2 μM $[Ca^{2+}]_i$ with 120 mM NaCl in the internal solution, and 30 mM NaCl (**d**) or 120 mM NaSCN (**e**) in the external solution; n= 5 for each point. (**f**) Population steady-state current density-voltage relationships from HEK293 cells expressing WT bBest2 in the presence of 1.2 μM $[Ca^{2+}]_i$ with 120 and 30 mM NaCl in the internal and external solutions, respectively. Results from solutions buffered with NMDG (open circle) were compared to those from solutions buffered with NaOH (solid circle, the same data set as in d); n= 5–6 for each point. (**g**) Population steady-state current density-voltage relationships from HEK293 cells expressing WT bBest2 in the presence of 1.2 μM $[Ca^{2+}]_i$ with 120 mM NMDG-Cl and $NMDG-CH_3SO_3$ in the internal and external solutions, respectively (open circle), compared to results from 120 mM NaCl and $NaCH_3SO_3$ in the internal and external solutions, respectively (solid circle); n= 5–6 for each point. (**h**) Reversal potentials from HEK293 cells expressing bBest2 WT, 3A, H91A, G199A, K208A and K265A. n= 5–18 for each point, the same color labels as in Figure 3d. The graphs are plotted using the same set of data as in Figure 3 and 7. All error bars in this figure represent s.e.m.
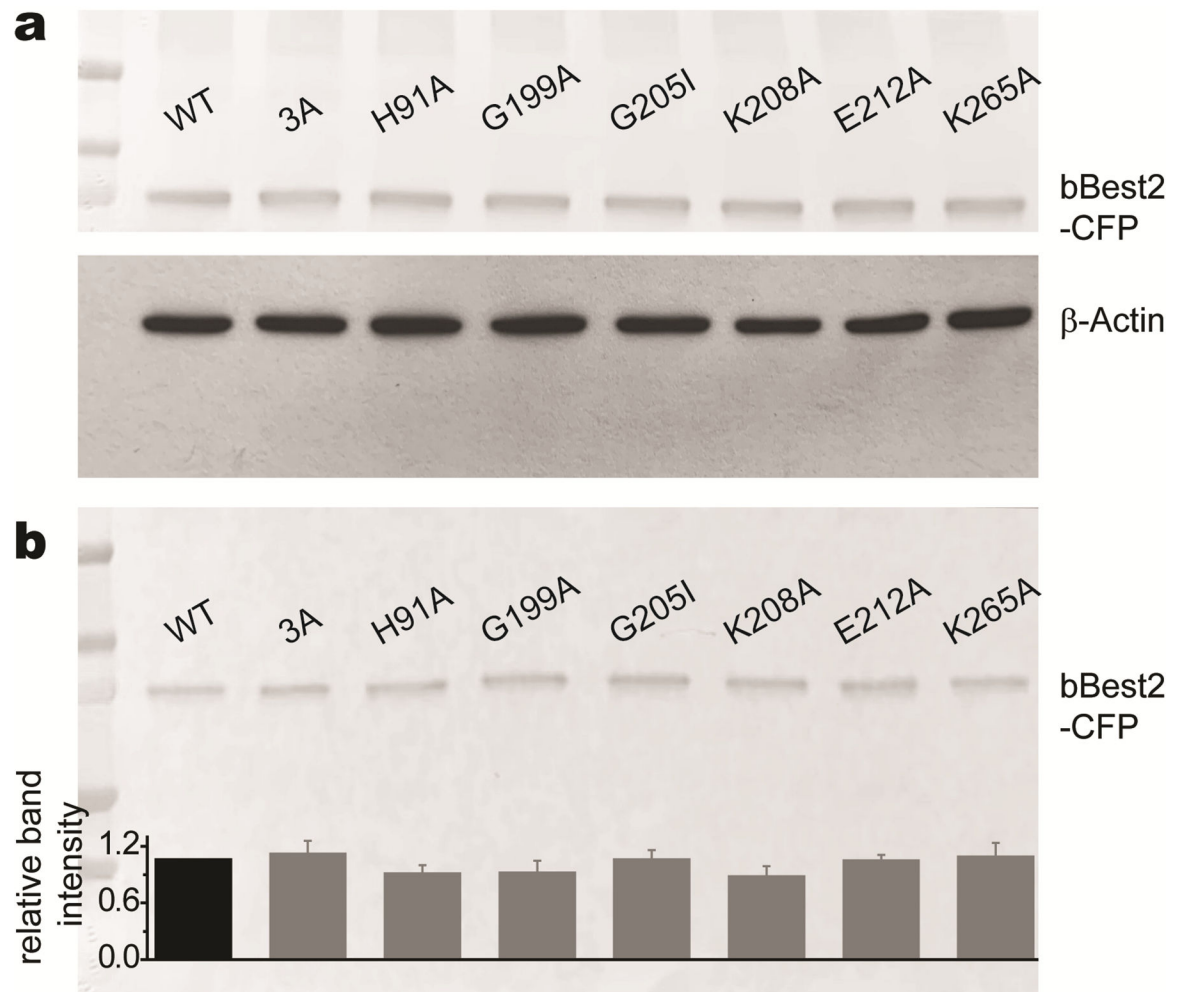
Extended Data Fig. 7. Expression and membrane trafficking of bBest2 mutants.
(**a**) *Top*, Western blot showing the transient expression levels of bBest2 WT and mutants in HEK293 whole-cell lysate; *Bottom*, β-Actin loading control from the same gel. (**b**) *Top*, cell surface expression levels of bBest2 WT and mutants in HEK293 cells were detected by immunoblotting. Membrane extractions were generated from the same batch of cell pellets as in **a**; *Bottom*, quantitation of the levels of bBest2 in plasma membrane from three independent experiments. Data were normalized to the global bBest2 level and then compared to WT. All error bars in this figure represent s.e.m.
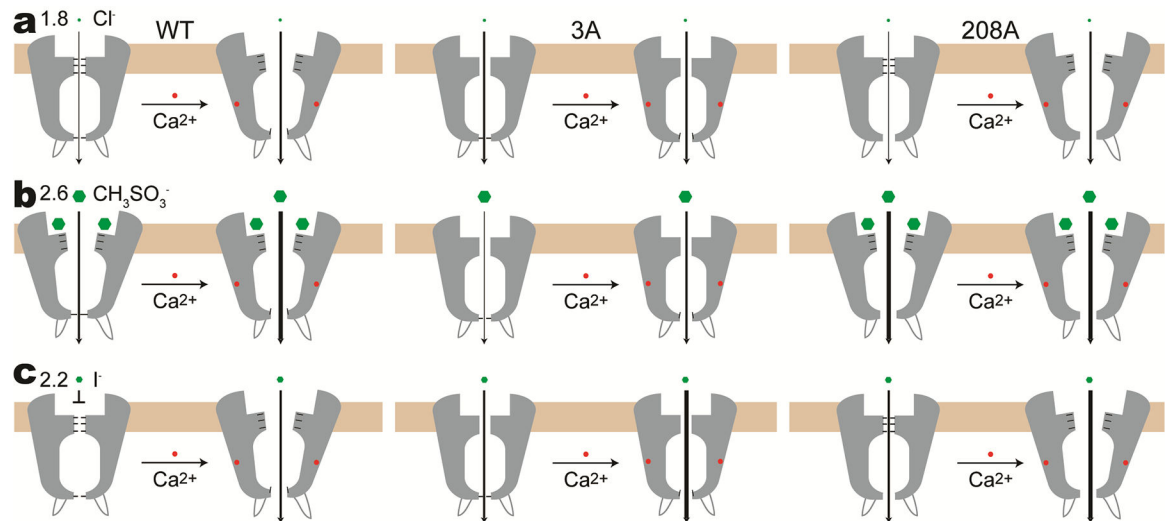
Extended Data Fig. 8. A two-gate activation model of bBest2.
(**a–c**) Cartoon showing the effect of Ca^{2+} on the permeation of Cl^- (**a**), $CH_3SO_3^-$ (**b**) and I^-
(**c**). The number indicates the radius (Å) of the dehydrated anion. The thickness of the
arrows reflect conductance of the channel.
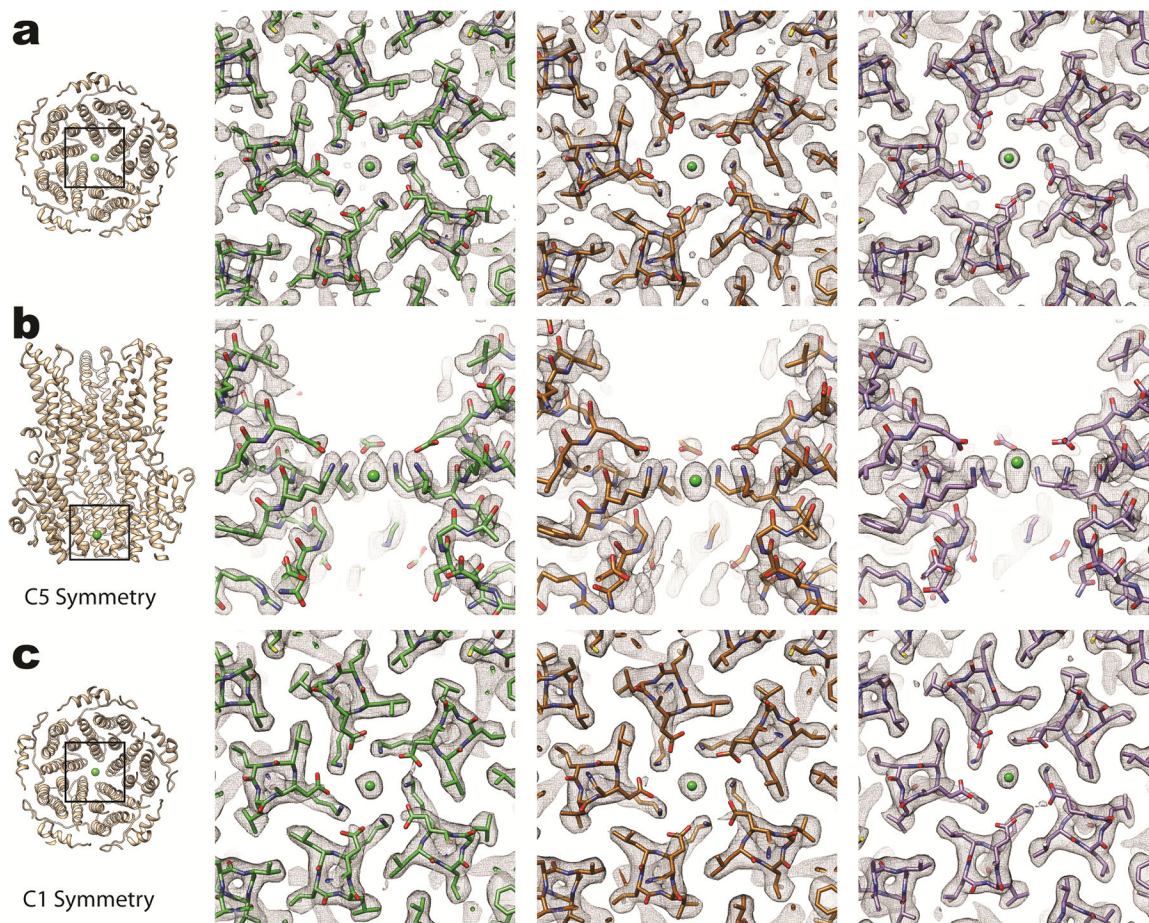
Extended Data Fig. 9. A putative anion binding site within the aperture of bBest2.
Left, the molecular model of bBest2. *Right*, representative map densities with the corresponding atomic model for EGTA Ca^{2+}-unbound state 1 (green), EGTA Ca^{2+}-unbound state 2 (pumpkin), and 5 mM Ca^{2+}-bound state (purple). (**a**) Map processed with C5 symmetry, view from inside the channel towards the aperture, as depicted in the ribbon cartoon (*left*). (**b**) Map processed with C5 symmetry, view from the side of the aperture, sliced to exclude one protomer, as depicted in the ribbon cartoon (*left*). (**c**) Map processed with C1 symmetry using the same particle set as its respective C5 map above, same view as in **a**.

Supplementary Material

Refer to Web version on PubMed Central for supplementary material.

Acknowledgments

References

1. Hartzell HC, Qu Z, Yu K, Xiao Q & Chien LT Molecular physiology of bestrophins: multifunctional membrane proteins linked to best disease and other retinopathies. Physiol Rev 88, 639–72 (2008). [PubMed: 18391176]

2. Xiao Q, Hartzell HC & Yu K Bestrophins and retinopathies. Pflugers Arch 460, 559–69 (2010). [PubMed: 20349192]

3. Sun H, Tsunenari T, Yau KW & Nathans J The vitelliform macular dystrophy protein defines a new family of chloride channels. Proc Natl Acad Sci U S A 99, 4008–13 (2002). [PubMed: 11904445]

4. Tsunenari T et al. Structure-function analysis of the bestrophin family of anion channels. J Biol Chem 278, 41114–25 (2003). [PubMed: 12907679]

5. Marmorstein AD et al. Bestrophin, the product of the Best vitelliform macular dystrophy gene (VMD2), localizes to the basolateral plasma membrane of the retinal pigment epithelium. Proc Natl Acad Sci U S A 97, 12758–63 (2000). [PubMed: 11050159]

6. Marquardt A et al. Mutations in a novel gene, VMD2, encoding a protein of unknown properties cause juvenile-onset vitelliform macular dystrophy (Best's disease). Hum Mol Genet 7, 1517–25 (1998). [PubMed: 9700209]

7. Petrukhin K et al. Identification of the gene responsible for Best macular dystrophy. Nat Genet 19, 241–7 (1998). [PubMed: 9662395]

8. Allikmets R et al. Evaluation of the Best disease gene in patients with age-related macular degeneration and other maculopathies. Hum Genet 104, 449–53 (1999). [PubMed: 10453731]

9. Burgess R et al. Biallelic mutation of BEST1 causes a distinct retinopathy in humans. Am J Hum Genet 82, 19–31 (2008). [PubMed: 18179881]

10. Davidson AE et al. Missense mutations in a retinal pigment epithelium protein, bestrophin-1, cause retinitis pigmentosa. Am J Hum Genet 85, 581–92 (2009). [PubMed: 19853238]

11. Ji C et al. Investigation and Restoration of BEST1 Activity in Patient-derived RPEs with Dominant Mutations. Sci Rep 9, 19026 (2019). [PubMed: 31836750]

12. Kramer F et al. Mutations in the VMD2 gene are associated with juvenile-onset vitelliform macular dystrophy (Best disease) and adult vitelliform macular dystrophy but not age-related macular degeneration. Eur J Hum Genet 8, 286–92 (2000). [PubMed: 10854112]

13. Yang T, Justus S, Li Y & Tsang SH BEST1: the Best Target for Gene and Cell Therapies. Mol Ther 23, 1805–9 (2015). [PubMed: 26388462]

14. Yardley J et al. Mutations of VMD2 splicing regulators cause nanophthalmos and autosomal dominant vitreoretinochoroidopathy (ADVIRC). Invest Ophthalmol Vis Sci 45, 3683–9 (2004). [PubMed: 15452077]

15. Bakall B et al. Bestrophin-2 is involved in the generation of intraocular pressure. Invest Ophthalmol Vis Sci 49, 1563–70 (2008). [PubMed: 18385076]

16. Zhang Y, Patil RV & Marmorstein AD Bestrophin 2 is expressed in human non-pigmented ciliary epithelium but not retinal pigment epithelium. Mol Vis 16, 200–6 (2010). [PubMed: 20157619]

17. Heijl A, Leske MC, Bengtsson B, Hyman L & Hussein M Reduction of intraocular pressure and glaucoma progression: results from the Early Manifest Glaucoma Trial. Arch Ophthalmol 120, 1268–79 (2002). [PubMed: 12365904]

18. Kass MA et al. The Ocular Hypertension Treatment Study: a randomized trial determines that topical ocular hypotensive medication delays or prevents the onset of primary open-angle glaucoma. Arch Ophthalmol 120, 701–13; discussion 829–30 (2002). [PubMed: 12049574]

19. Lichter PR et al. Interim clinical outcomes in the Collaborative Initial Glaucoma Treatment Study comparing initial treatment randomized to medications or surgery. Ophthalmology 108, 1943–53 (2001). [PubMed: 11713061]

20. Cui CY et al. Forkhead transcription factor FoxA1 regulates sweat secretion through Bestrophin 2 anion channel and Na-K-Cl cotransporter 1. Proc Natl Acad Sci U S A 109, 1199–203 (2012). [PubMed: 22223659]

21. Yu K, Lujan R, Marmorstein A, Gabriel S & Hartzell HC Bestrophin-2 mediates bicarbonate transport by goblet cells in mouse colon. J Clin Invest 120, 1722–35 (2010). [PubMed: 20407206]

22. Kane Dickson V, Pedi L & Long SB Structure and insights into the function of a Ca(2+)-activated Cl(−) channel. Nature 516, 213–8 (2014). [PubMed: 25337878]

23. Yang T et al. Structure and selectivity in bestrophin ion channels. Science 346, 355–9 (2014). [PubMed: 25324390]

24. Vaisey G, Miller AN & Long SB Distinct regions that control ion selectivity and calcium-dependent activation in the bestrophin ion channel. Proc Natl Acad Sci U S A 113, E7399–E7408 (2016). [PubMed: 27821745]

25. Zhang Y et al. ATP activates bestrophin ion channels through direct interaction. Nat Commun 9, 3126 (2018). [PubMed: 30087350]

26. Qu Z, Chien LT, Cui Y & Hartzell HC The anion-selective pore of the bestrophins, a family of chloride channels associated with retinal degeneration. J Neurosci 26, 5411–9 (2006). [PubMed: 16707793]

27. Qu Z, Fischmeister R & Hartzell C Mouse bestrophin-2 is a bona fide Cl(−) channel: identification of a residue important in anion binding and conduction. J Gen Physiol 123, 327–40 (2004). [PubMed: 15051805]

28. Qu Z & Hartzell C Determinants of anion permeation in the second transmembrane domain of the mouse bestrophin-2 chloride channel. J Gen Physiol 124, 371–82 (2004). [PubMed: 15452198]

29. Li Y et al. Patient-specific mutations impair BESTROPHIN1's essential role in mediating Ca2+-dependent Cl- currents in human RPE. Elife 6(2017).

30. Qu Z, Wei RW, Mann W & Hartzell HC Two bestrophins cloned from Xenopus laevis oocytes express Ca(2+)-activated Cl(−) currents. J Biol Chem 278, 49563–72 (2003). [PubMed: 12939260]

31. Ji C et al. Dual Ca(2+)-dependent gates in human Bestrophin1 underlie disease-causing mechanisms of gain-of-function mutations. Commun Biol 2, 240 (2019). [PubMed: 31263784]

32. Miller AN, Vaisey G & Long SB Molecular mechanisms of gating in the calcium-activated chloride channel bestrophin. Elife 8(2019).

33. Civan MM, Peterson-Yantorno K, Sanchez-Torres J & Coca-Prados M Potential contribution of epithelial Na+ channel to net secretion of aqueous humor. J Exp Zool 279, 498–503 (1997). [PubMed: 9392872]

34. Jacob TJ & Civan MM Role of ion channels in aqueous humor formation. Am J Physiol 271, C703–20 (1996). [PubMed: 8843699]

35. Qu Z & Hartzell HC Bestrophin Cl- channels are highly permeable to HCO3. Am J Physiol Cell Physiol 294, C1371–7 (2008). [PubMed: 18400985]

36. Frings S, Reuter D & Kleene SJ Neuronal Ca2+ -activated Cl- channels--homing in on an elusive channel species. Prog Neurobiol 60, 247–89 (2000). [PubMed: 10658643]

37. Kittredge A, Ward N, Hopiavuori A, Zhang Y & Yang T Expression and Purification of Mammalian Bestrophin Ion Channels. J Vis Exp (2018).

38. Suloway C et al. Automated molecular microscopy: the new Leginon system. J Struct Biol 151, 41–60 (2005). [PubMed: 15890530]

39. Rice WJ et al. Routine determination of ice thickness for cryo-EM grids. J Struct Biol 204, 38–44 (2018). [PubMed: 29981485]

40. Terwilliger TC, Ludtke SJ, Read RJ, Adams PD & Afonine PV Improvement of cryo-EM maps by density modification. bioRxiv (2019).

41. Zheng SQ et al. MotionCor2: anisotropic correction of beam-induced motion for improved cryo-electron microscopy. Nat Methods 14, 331–332 (2017). [PubMed: 28250466]

42. Zhang K Gctf: Real-time CTF determination and correction. J Struct Biol 193, 1–12 (2016). [PubMed: 26592709]

43. Kimanius D, Forsberg BO, Scheres SH & Lindahl E Accelerated cryo-EM structure determination with parallelisation using GPUs in RELION-2. Elife 5(2016).

44. Punjani A, Rubinstein JL, Fleet DJ & Brubaker MA cryoSPARC: algorithms for rapid unsupervised cryo-EM structure determination. Nat Methods 14, 290–296 (2017). [PubMed: 28165473]

45. Asarnow D, Palovcak E & Chen Y asarnow/pyem: UCSF pyem v0.5. (2019).

46. Zivanov J et al. New tools for automated high-resolution cryo-EM structure determination in RELION-3. Elife 7(2018).

47. Benkert P, Biasini M & Schwede T Toward the estimation of the absolute quality of individual protein structure models. Bioinformatics 27, 343–50 (2011). [PubMed: 21134891]

48. Bertoni M, Kiefer F, Biasini M, Bordoli L & Schwede T Modeling protein quaternary structure of homo- and hetero-oligomers beyond binary interactions by homology. Sci Rep 7, 10480 (2017). [PubMed: 28874689]

49. Bienert S et al. The SWISS-MODEL Repository-new features and functionality. Nucleic Acids Res 45, D313–D319 (2017). [PubMed: 27899672]

50. Guex N, Peitsch MC & Schwede T Automated comparative protein structure modeling with SWISS-MODEL and Swiss-PdbViewer: a historical perspective. Electrophoresis 30 Suppl 1, S162–73 (2009). [PubMed: 19517507]

51. Waterhouse A et al. SWISS-MODEL: homology modelling of protein structures and complexes. Nucleic Acids Res 46, W296–W303 (2018). [PubMed: 29788355]

52. Afonine PV et al. Real-space refinement in PHENIX for cryo-EM and crystallography. Acta Crystallogr D Struct Biol 74, 531–544 (2018). [PubMed: 29872004]

53. Emsley P & Cowtan K Coot: model-building tools for molecular graphics. Acta Crystallogr D Biol Crystallogr 60, 2126–32 (2004). [PubMed: 15572765]

54. Chen VB et al. MolProbity: all-atom structure validation for macromolecular crystallography. Acta Crystallogr D Biol Crystallogr 66, 12–21 (2010). [PubMed: 20057044]

55. Afonine PV et al. New tools for the analysis and validation of cryo-EM maps and atomic models. Acta Crystallogr D Struct Biol 74, 814–840 (2018). [PubMed: 30198894]

56. Barad BA et al. EMRinger: side chain-directed model and map validation for 3D cryo-electron microscopy. Nat Methods 12, 943–6 (2015). [PubMed: 26280328]

57. Heymann JB Guidelines for using Bsoft for high resolution reconstruction and validation of biomolecular structures from electron micrographs. Protein Sci 27, 159–171 (2018). [PubMed: 28891250]

58. Pettersen EF et al. UCSF Chimera--a visualization system for exploratory research and analysis. J Comput Chem 25, 1605–12 (2004). [PubMed: 15264254]

59. Chovancova E et al. CAVER 3.0: a tool for the analysis of transport pathways in dynamic protein structures. PLoS Comput Biol 8, e1002708 (2012). [PubMed: 23093919]

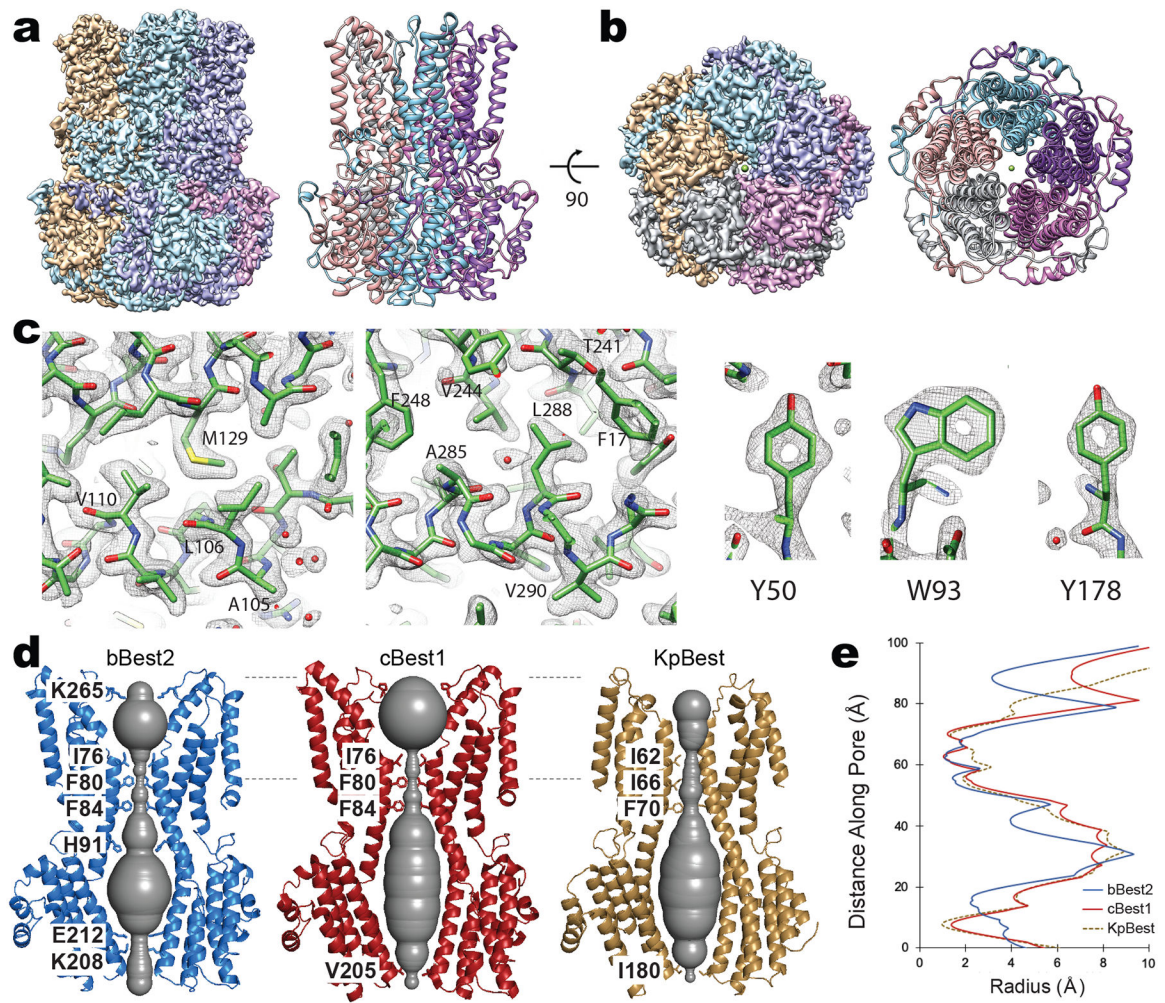**Figure 1. Cryo-EM structure of bBest2 and comparison to cBest1 and KpBest.**
(**a**) Side view of cryo-EM density map (Ca^{2+}-bound state) at overall 2.4 Å resolution (*left*) and model (*right*). (**b**) Cytosolic view of cryo-EM density map (Ca^{2+}-bound state, *left*) and model (*right*). (**c**) Example densities from the Ca^{2+}-unbound (EGTA only) map exhibiting high resolution features, including carbonyl groups, water molecules (red spheres), and holes in aromatic groups. (**d**) Side view of two opposing (144°) protomers from each channel with the ion permeation pathway visualized as a solid surface by the Caver3.0 program. Major constrictions to the ion permeation pathway are shown as sticks with residue labels on the left. Dashed lines indicate approximate boundaries of the transmembrane domains. (**e**) Analysis of the ion permeation pathway radius (Ca^{2+}-bound state) as calculated by the HOLE program.
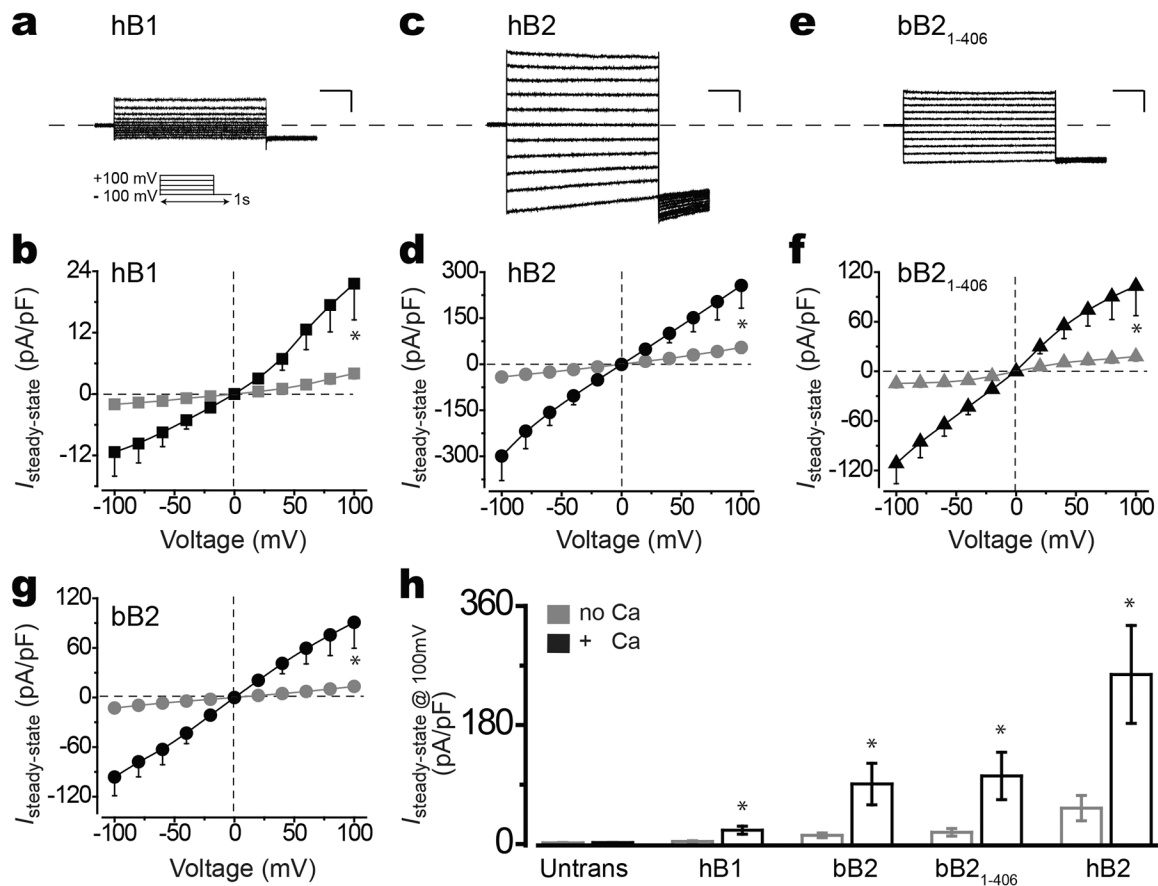
Figure 2. Ca^{2+}-dependent Cl$^-$ current mediated by Best1 and Best2.
(**a-f**) Representative current traces in the presence of 1.2 μM [Ca^{2+}]$_i$ (**a, c, e**), and population steady-state current density-voltage relationships (**b, d, f**) in the absence (gray) and presence (black) of 1.2 μM [Ca^{2+}]$_i$ from HEK293 cells expressing hBest1 (**a-b**), hBest2 (**c-d**) or bBest2$_{1-406}$ (**e-f**); n= 5–6 for each point. *P< 0.05 compared to currents without Ca^{2+}, using two-tailed unpaired Student t test. Scale bar, 300 pA (**a**), 1 nA (**c, e**), and 150 ms (**a, c, e**). Voltage protocol used to elicit currents is shown in *Inset*. (**g**) Population steady-state current density-voltage relationships from HEK293 cells expressing bBest2 in the absence (gray) and presence (black) of 1.2 μM [Ca^{2+}]$_i$; n= 10–12 for each point. *P< 0.05 compared to currents without Ca^{2+}, using two-tailed unpaired Student t test. (**h**) Bar chart showing the steady-state current densities from HEK293 cells expressing the indicated channels in the absence and presence of 1.2 μM [Ca^{2+}]$_i$, n= 5–12 for each bar. *P< 0.05 compared to currents without Ca^{2+} under the same condition, using two-tailed unpaired Student t test. All error bars in this figure represent s.e.m. Data are available as Source Data 1.
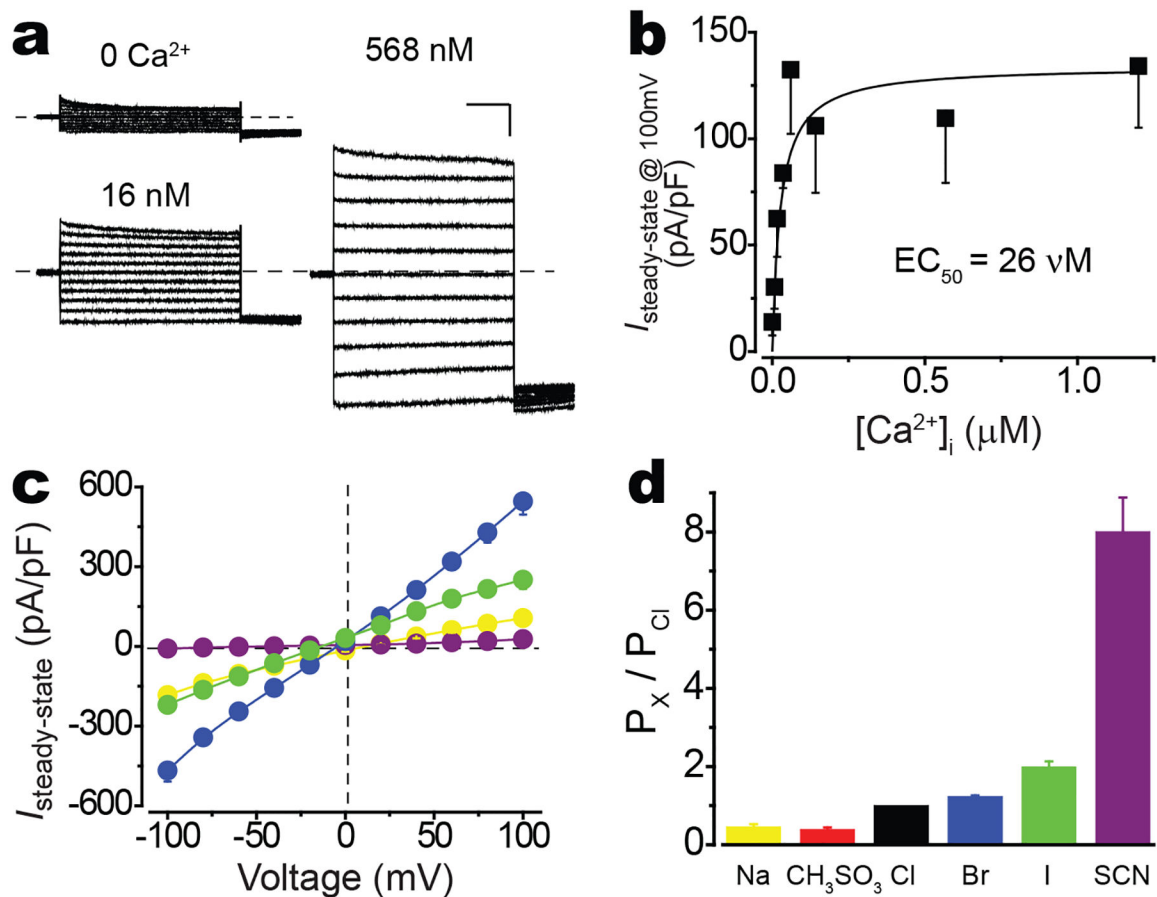
Figure 3. Ca²⁺-dependence and ion selectivity of bBest2.

(**a**) Representative current traces recorded from HEK293 cells expressing bBest2 at various free $[Ca^{2+}]_i$s. Scale bar, 350 pA, 150 ms. (**b**) Ca^{2+}-dependent channel activity. Steady-state current density was recorded at +100 mV plotted vs. free $[Ca^{2+}]_i$ and fitted to the Hill equation (solid line); n= 5–6 for each point. (**c**) Population steady-state current density-voltage relationships with substituted external solutions; n= 5–8 for each point. Blue: 120 mM NaBr, green: 120 mM NaI, purple: 120 mM NaSCN, yellow: 30 mM NaCl in the external solutions. (**d**) Relative ion permeability ratios (P_X/P_{Cl}) of bBest2. P_X/P_{Cl} was calculated from the Goldman-Hodgkin-Katz equation taking P_{Na}/P_{Cl} into account. Same colors as **c**. Red: 120 mM $NaCH_3SO_3$, and black: 120 mM NaCl in the external solutions. All error bars in this figure represent s.e.m. Data are available as Source Data 2.
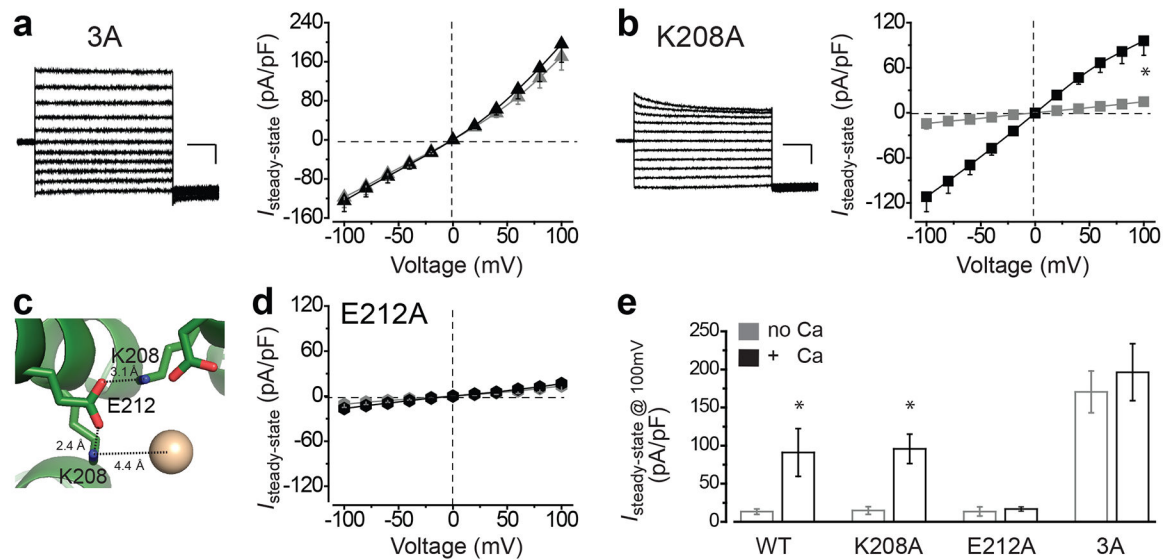
Figure 4. The role of the neck and aperture in Ca^{2+}-dependent gating of Cl$^-$.
(**a, b**) Representative current traces in the presence of 1.2 μM [Ca^{2+}]$_i$, and population steady-state current density-voltage relationships in the absence (gray) and presence (black) of 1.2 μM [Ca^{2+}]$_i$ from HEK293 cells expressing bBest2 3A (**a**) or K208A (**b**); n= 13–19 for each point. *P< 0.05 compared to currents without Ca^{2+}, using two-tailed unpaired Student t test. Scale bar, 500 pA, 150 ms. (**c**) Interactions between K208 and E212 at the aperture. Dotted black lines illustrate salt bridges. Brown dot, a Cl$^-$ ion. (**d**) Population steady-state current density-voltage relationships from HEK293 cells expressing bBest2 E212A in the absence (gray) and presence (black) of 1.2 μM [Ca^{2+}]$_i$; n= 10–11 for each point. (**e**) Bar chart showing the steady-state current densities from HEK293 cells expressing the indicated bBest2 derivatives in the absence and presence of 1.2 μM [Ca^{2+}]$_i$, n= 10–19 for each bar. *P < 0.05 compared to currents without Ca^{2+} under the same condition, using two-tailed unpaired Student t test. All error bars in this figure represent s.e.m. Data are available as Source Data 3.
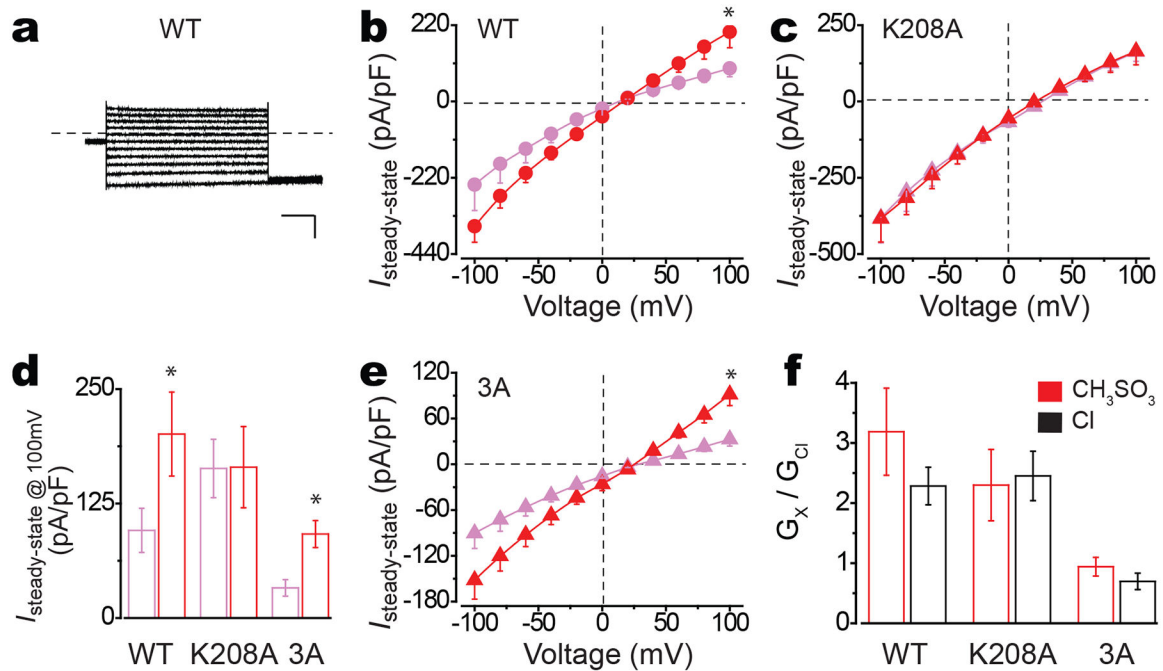
Figure 5. The role of the neck and aperture in Ca²⁺-dependent gating of CH₃SO3-.
(**a**) Representative WT current traces in the presence of 1.2 μM $[Ca^{2+}]_i$, with $CH_3SO_3^-$ in the external solution. Scale bar, 1.5 nA, 150 ms. (**b, c**) Population steady-state current density-voltage relationships from HEK293 cells expressing the WT bBest2 (**b**) or the K208A mutant (**c**) in the absence (light magenta) and presence (red) of 1.2 μM $[Ca^{2+}]_i$; n= 5–12 for each point. *$P < 0.05$ compared to currents without Ca^{2+}, using two-tailed unpaired Student t test. (**d**) Bar chart showing the steady-state current densities from HEK293 cells expressing the indicated bBest2 derivatives in the absence (light magenta) and presence (red) of 1.2 μM $[Ca^{2+}]_i$, n= 5–18 for each bar. *$P < 0.05$ compared to currents without Ca^{2+} under the same condition, using two-tailed unpaired Student t test. (**e**) Population steady-state current density-voltage relationships from HEK293 cells expressing bBest2 3A in the absence (light magenta) and presence (red) of 1.2 μM $[Ca^{2+}]_i$; n= 14–18 for each point. *$P < 0.05$ compared to currents without Ca^{2+}, using two-tailed unpaired Student t test. (**f**) Relative ion conductance ratios (G_X/G_{Cl}) measured as slope conductance at the reversal potential plus 50 mV ($CH_3SO_3^-/Cl^-$, red) or minus 50 mV (Cl^-/Cl^-, black) in the presence of 1.2 μM $[Ca^{2+}]_i$, n= 5–18 for each bar. All error bars in this figure represent s.e.m. Data are available as Source Data 4.

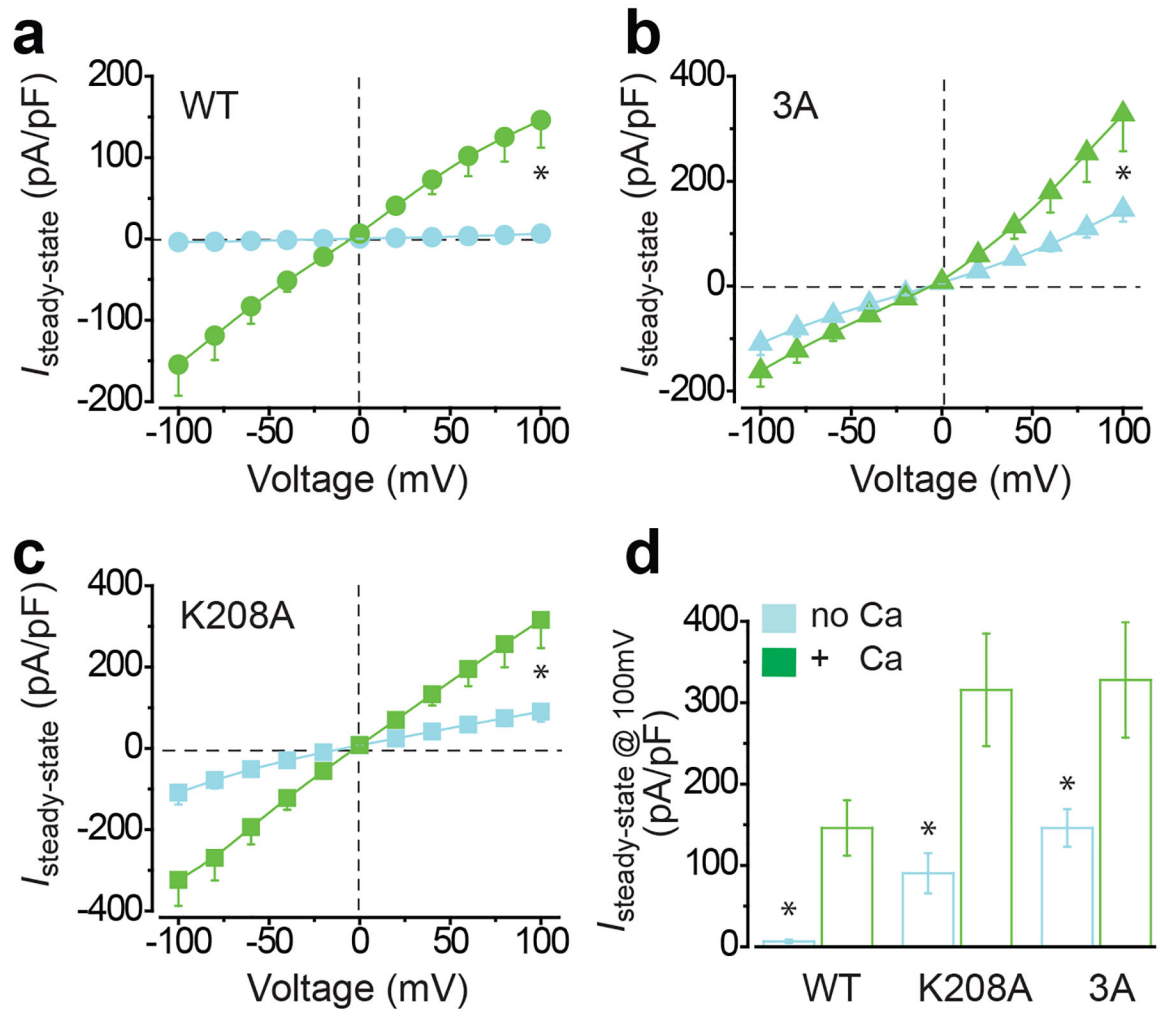**Figure 6. The role of the neck and aperture in Ca^{2+}-dependent gating of I^{-}.**
(**a-c**) Population steady-state current density-voltage relationships from HEK293 cells expressing bBest2 WT (**a**), 3A (**b**) or K208A (**c**) in the absence (light cyan) and presence (green) of 1.2 μM [Ca^{2+}]$_i$; n= 6–18 for each point. *$P < 0.05$ compared to currents without Ca^{2+}, using two-tailed unpaired Student t test. (**d**) Bar chart showing the steady-state current densities in the absence and presence of 1.2 μM [Ca^{2+}]$_i$, n= 6–18 for each bar. *$P < 0.05$ compared to currents with Ca^{2+} under the same condition, using two-tailed unpaired Student t test. All error bars in this figure represent s.e.m. Data are available as Source Data 5.
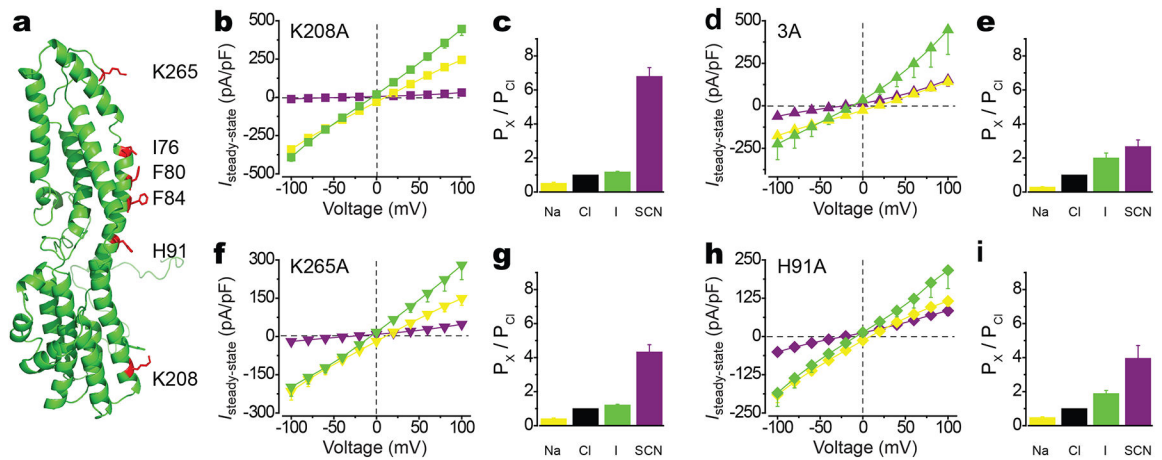
Figure 7. Critical residues for the ion selectivity of bBest2.
(**a**) Ribbon diagram of a bBest2 protomer is shown with the extracellular side on the top. The side chains of critical residues are in red. (**b-i**) Population steady-state current density-voltage relationships with substituted external solutions (**b, d, f, h**), and relative ion permeability ratios (P_X/P_{Cl}) (**c, e, g, i**) from HEK293 cells expressing bBest2 K208A (**b, c**), 3A (**d, e**), K265A (**f, g**) or H91A (**h, i**). P_X/P_{Cl} was calculated from the Goldman-Hodgkin-Katz equation taking P_{Na}/P_{Cl} into account. n= 5–18 for each point, the same color labels as in Figure 3d. Data are available as Source Data 6.

Table 1.

Cryo-EM data collection, refinement and validation statistics

	bestrophin-2 Ca²⁺-unbound state 1 (EGTA only) (EMD-21434, PDB 6VX9)	bestrophin-2 Ca²⁺-unbound state 2 (EGTA only) (EMD-21433, PDB 6VX8)	bestrophin-2 Ca²⁺-bound state (5 mM Ca²⁺) (EMD-21432, PDB 6VX7)	bestrophin-2 Ca²⁺-bound state (250 nM Ca²⁺) (EMD-21431, PDB 6VX6)	bestrophin-2 Ca²⁺-unbound state (250 nM Ca²⁺) (EMD-21430, PDB 6VX5)
Data collection and processing					
Magnification	22,500	22,500	105,000	29,000	29,000
Voltage (kV)	300	300	300	300	300
Electron exposure (e⁻/Å²)	69.67	69.67	58.00	73.14	73.14
Defocus range (μm)	0.8–1.5	0.8–1.5	0.8–1.4	1.5–2.5	1.5–2.5
Pixel size (Å)	1.07	1.07	0.83	0.83	0.83
Symmetry imposed	C5	C5	C5	C5	C5
Initial particle images (no.)	3,714,156	3,714,156	3,734,960	5,236,545	5,236,545
Final particle images (no.)	280,524	120,642	332,270	18,971	14,376
Map resolution (Å)	2.17	2.33	2.36	3.00	3.03
FSC threshold	0.143	0.143	0.143	0.143	0.143
Map resolution range (Å)	2.15–5.50	2.15–6.20	2.20–6.00	2.50–9.00	2.50–10.00
Refinement					
Initial model used (PDB code)	6VX6	6VX6	6VX6	4RDQ	6VX6
Model resolution (Å)	2.21	2.46	2.50	3.14	3.28
FSC threshold	0.5	0.5	0.5	0.5	0.5
Model composition					
Nonhydrogen atoms	15,471	13,816	15,526	15,061	13,056
Protein residues	1,825	1,620	1,830	1,830	1,575
Ligands	1 (Cl⁻)	1 (Cl⁻)	6 (5 Ca²⁺, 1 Cl⁻)	6 (5 Ca²⁺, 1 Cl⁻)	1 (Cl⁻)
B factors (Å²)					
Protein	34.46	33.21	9.09	58.99	123.48
Ligand	22.59	50.00	2.59	50.00	50.00
R.m.s. deviations					
Bond lengths (Å)	0.009 (0)	0.010 (0)	0.008 (0)	0.005 (0)	1.106 (0)
Bond angles (°)	1.268 (0)	1.300 (0)	1.003 (0)	1.126 (5)	0.007 (0)
Validation					
MolProbity score	1.65	1.79	1.80	1.24	1.46
Clashscore	7.07	7.43	5.78	4.74	4.78
Poor rotamers (%)	0.95	2.86	2.52	0.94	0.22
Ramachandran plot					
Favored (%)	96.14	97.83	96.98	98.08	96.61
Allowed (%)	3.86	2.17	3.02	1.92	3.39
Disallowed (%)	0	0	0	0	0